Science Advances
AAAS

# Manuscript Template

## FRONT MATTER

### Title

· A biomineral-inspired approach of synthesizing colloidal persistent phosphors as a multicolor, intravital light source
· Bioinspired nanophosphors for afterglow imaging

### Authors

Fan Yang[1,2]†, Xiang Wu[1,2]†, Han Cui[1,2], Zihao Ou[1,2], Shan Jiang[1,2], Sa Cai[1,2], Qi Zhou[1,2], Bryce G. Wong[1,2], Hans Huang[1,2], and Guosong Hong[1,2]*

### Affiliations

[1] Department of Materials Science and Engineering, Stanford University, Stanford, CA, 94305, USA
[2] Wu Tsai Neurosciences Institute, Stanford University, Stanford, CA, 94305, USA
† These authors contributed equally to this work.
* Corresponding author: guosongh@stanford.edu

### Abstract

Many *in vivo* biological techniques, such as fluorescence imaging, photodynamic therapy, and optogenetics, require light delivery into biological tissues. The limited tissue penetration of visible light discourages the use of external light sources and calls for the development of light sources that can be delivered *in vivo*. A promising material for internal light delivery is persistent phosphors; however, there is a scarcity of materials with strong persistent luminescence of visible light in a stable colloid to facilitate systemic delivery *in vivo*. Here, we used a bioinspired demineralization (BID) strategy to synthesize stable colloidal solutions of solid-state phosphors in the range of 470-650 nm and diameters down to 20 nm. The exceptional brightness of BID-produced colloids enables their utility as multicolor luminescent tags *in vivo* with favorable biocompatibility. Owing to their stable dispersion in water, BID-produced nanophosphors can be delivered systemically, acting as an intravascular colloidal light source to internally excite genetically encoded fluorescent reporters within the mouse brain.

### Teaser

A bioinspired approach produces bright afterglow colloids that can excite endogenous fluorescent proteins for brain imaging.

## MAIN TEXT

## Introduction

Light is used in a wide range of methods in biology and medicine, such as fluorescence imaging (*1*), optogenetics (*2*), photoactivatable gene editing (*3*), light-controlled immunotherapy (*4*), and photochemotherapy for cancers and viral infections (*5*). A critical challenge of applying light *in vivo*, such as deep-brain imaging and optogenetics, arises from the poor penetration of photons in biological tissue due to scattering and absorption (*1*). Therefore, delivering photons deep into the body from an external light source requires invasive procedures, such as craniotomy to surgically remove overlying tissues.

Besides conventionally used external light sources, internally delivered light sources represent an arising opportunity to mitigate the challenges associated with the poor tissue penetration of photons. On one hand, nanofabricated light sources in a flexible and stretchable platform provide a minimally invasive strategy for delivering an internal light source *in vivo* (*6*, *7*). On the other hand, microparticles and nanoparticles with persistent luminescence, also known as the afterglow, represent another potential approach for internal light delivery owing to their ability to store photon energy in their chemical structures. Although afterglow imaging with these materials has attracted substantial research interest (*8–10*), conventional afterglow materials emit red to near-infrared (NIR) light to facilitate imaging with deep tissue penetration (*8*, *9*, *11*). In contrast, materials with a strong afterglow in the short-wavelength visible spectrum are needed to fulfill their roles as a light source to excite fluorescent proteins, opsins, photoswitchable Cas9 (psCas9), etc., due to the activation spectrum of these proteins in the visible range (*2*, *12*, *13*). In addition, these short-wavelength light sources must have good colloidal stability in physiological aqueous environments to facilitate their delivery *in vivo*, preferably via the circulatory system. Despite recent efforts in developing short-wavelength afterglow materials for biological applications (*14*, *15*), the decay lifetimes and brightness of these materials remain to be improved. Thus, there is still a scarcity of afterglow nanomaterials with long lifetimes, sufficiently short wavelengths (especially blue), and colloidal stability to enable *in vivo* use as an internal light source.

We argue that the lack of short-wavelength afterglow colloids reflects an intrinsic gap between wet-chemical and solid-state reactions for synthesizing persistent luminescence phosphors. On one hand, wet-chemical approaches (e.g., the sol-gel method) have enabled the synthesis of chromium-doped gallate ($ZnGa_2O_4:Cr^{3+}$, 695 nm), semiconducting polymers (780 nm), and rare-earth doped nanoparticles ($NaLnF_4$:RE, >1,000 nm) with sufficient brightness and biocompatibility for deep-tissue afterglow imaging (*8–10*, *16–19*). However, the long wavelengths of these materials are energetically unfavorable to excite fluorescent proteins, opsins, and psCas9. It is hypothesized that point defects necessary for strong persistent luminescence in the short-wavelength visible spectrum are thermodynamically and kinetically unfavorable to form at low processing temperatures, thus making conventional sol-gel methods incapable of synthesizing blue-shifted afterglow nanoparticles (*20*). On the other hand, solid-state reactions enable the synthesis of inorganic phosphors with tunable wavelengths down to 400 nm and strong persistent luminescence by facilitating uniform doping of color centers in host materials of desirable polymorphs (*21*). However, solid-state-synthesized phosphors remain refractory to wet chemical methods; moreover, their large sizes (>10 μm) prohibit their use in a living body (*20*). Although mechanical milling represents a plausible route to produce nanoparticles from solid-state products, the plastic deformation process introduces undesired built-in stresses and dislocations into the resulting nanoparticles (*22*). These built-in stresses and dislocations lead to mechanical quenching and defect-induced quenching of milled phosphor nanoparticles (*23*, *24*), thus making mechanical

milling an unfavorable approach for producing colloidal light sources from solid-state precursor particles.

Here we report a bioinspired demineralization (BID) approach to synthesize stable colloidal solutions of solid-state phosphors with tunable wavelengths and remarkable afterglow intensity. The BID approach is a generalizable wet-chemical method to produce colloidal nanophosphors from high-temperature, solid-state reactions, thus bridging the gap between these two conventional, yet mutually incompatible strategies (i.e., sol-gel vs solid-state) discussed above. Additionally, the BID approach is a much more mild alternative to mechanical milling, thereby avoiding the built-in stress and dislocations induced during milling that would otherwise quench the afterglow. Specifically, the BID approach is inspired by the strategy of biomineralization in Nature: biominerals, such as apatite in the dental enamel, can be gradually dissolved to nanostructures in a mildly acidic environment yet are resistant to further dissolution (*25*). In this work, we demonstrate that the kinetic stability of nanostructures is also prevalent in solid-state phosphors and apply this universal strategy to a wide array of phosphors. Specifically, the BID approach can produce stable colloidal solutions of silicates, aluminates, and sulfides with diameters down to 20 nm and afterglow wavelengths from 470 nm to 650 nm. These nanophosphor colloids preserve the high crystallinity, bright luminescence, long afterglow, and specific wavelength of their micron-sized precursors from solid-state reactions. We demonstrate these water-soluble materials as colloidal light sources that can be delivered via intravenous injection, enabling internal excitation of genetically encoded fluorescent proteins *in vivo* with advanced tissue penetration.

## Results

### A bioinspired demineralization approach of producing colloidal solutions of nanophosphors

Satisfying the requirement for bright luminescence and tunable wavelengths prohibits the use of sol-gel methods and necessitates solid-state reactions at elevated temperatures to produce persistent phosphors with desired point defects in host materials of specific phases (*20*). However, solid-state phosphors prepared at high temperatures are usually >10 μm particles composed of water-insoluble materials. As discussed in the Introduction, these solid-state phosphors are refractory to ball milling due to mechanical and dislocation-induced quenching effects. To mitigate this challenge, we leveraged a unique phenomenon found in Nature in the process of demineralization. Demineralization of naturally occurring biominerals (e.g., tooth enamel, seashells, etc.) features a self-preservation behavior, which exhibits the kinetic stability of biomineral nanoparticles in an aqueous solution despite their thermodynamic metastable nature (*25*, *26*). We hypothesize that this kinetic stability of nanostructures is also applicable to solid-state phosphors with a low water-solubility, such as sparingly soluble silicates and aluminates (Fig. 1A) (*27*, *28*). This kinetic stability despite thermodynamic metastability is the basis of the BID technique.

Specifically, the BID technique contrasts conventional wet chemical etching, which usually exhibits self-accelerating dissolution (such as the dissolution of a cane sugar crystal in water). Smaller particles possess higher specific surface energy and thus greater solubility than larger ones, which is well known as Ostwald ripening (*29*). This behavior prohibits the use of conventional wet chemical etching to produce a stable colloidal solution of persistent phosphors, especially those <50 nm, without complete dissolution of the colloids. In contrast, biominerals, which share similar chemical compositions and sparing solubility as solid-state phosphors, exhibit suppressed dissolution of their nanosized crystallites in undersaturated solutions (*25*, *26*). Specifically, the dissolution of biominerals is facilitated by the formation and growth of pits on the surfaces. It has

been theoretically predicted and experimentally validated that the rate of dissolution, $R$, is related to the radius of the pit, $r$, as follows (*27*):

$$R = R_{\infty}(1 - \frac{r^*}{r}) \quad (1)$$

where $R_{\infty}$ is the dissolution rate at $r \rightarrow \infty$, which is usually achieved in bulk material. $r^*$ is the critical radius of the pit, which determines the size of kinetically preserved nanoparticles and is related to the surface energy and Gibbs free energy of dissolution as follows:

$$r^* = -\frac{\gamma_{SL}\Omega}{\Delta g} \quad (2)$$

Here, $\gamma_{SL}$ represents the interfacial tension of a solid in the solution, $\Omega$ is the surface area of each dissolution unit, and $\Delta g$ is the Gibbs free energy of dissolution per dissolution unit. Sparingly soluble solids such as biominerals and inorganic phosphors always have much larger interfacial tension than soluble salts (*30*), thus resulting in large values of $r^*$ in the range of 10-100 nm. Therefore, we hypothesize that this bioinspired demineralization approach can provide a generalizable method to produce nanophosphors with targeted size distributions determined by $r^*$ (Fig. 1A).

In the BID process, we used a citrate buffer to mimic the undersaturated environment that etches biominerals to produce colloid solutions of solid-state nanophosphors (see Materials and Methods). Citrate buffer at pH<10 provides a negative $\Delta g$ to satisfy eq. (2) (fig. S1-5) instead of serving the role of a surfactant in conventional mechanical milling methods. We selected strontium magnesium silicate doped with $Eu^{2+}$ and $Dy^{3+}$ ($Sr_2MgSi_2O_7$:Eu,Dy, SMSO) as a representative example of persistent phosphors, owing to its strong and long-lasting blue afterglow that provides excitation for many light-activated proteins such as the yellow fluorescent protein (YFP), stable step-function opsins (SSFO), and psCas9 (*3*, *12*, *13*, *31*). SMSO with a strong afterglow cannot be synthesized via a sol-gel method due to crystallinity and doping requirements, thus generally resulting in micron-sized particles that cannot form a stable colloidal suspension in water (*32*).

In our experiments, SMSO synthesized in solid-state reactions began with an average size of >10 μm, as evidenced by scanning electron microscope (SEM) images (Fig. 1B, i). The large size distribution of these SMSO microparticles prohibited a stable suspension in water, as evidenced by a blue afterglow from the precipitates instead of the supernatant (Fig. 1C, i). In contrast, the BID approach produced a stable colloidal solution of SMSO nanophosphors with a strong and uniform blue afterglow (Fig. 1C, ii) and a size distribution of 43 ± 11 nm (Fig. 1B, ii&iii & 1D). We used Fourier-transform infrared (FTIR) spectroscopy, nuclear magnetic resonance (NMR) spectroscopy, and UV-visible absorption spectroscopy to fully characterize the products of the BID process (fig. S1-5).

**Mechanistic study of the BID technique for producing colloidal solutions of nanophosphors**

We next sought to validate the mechanism of kinetic preservation to produce SMSO colloids. First, surface roughening represents a significant hallmark of the self-preserved demineralization process of biominerals (*25*). We compared the SEM images of large SMSO particles before and after the BID process (Fig. 1B, i and Fig. 1E). In contrast to the smooth surface before, SMSO particles after the BID process exhibited much rougher surfaces, featuring nanostructures such as particles and troughs with sizes ≤100 nm, similar to those found during natural demineralization. During surface roughening, every single micron-sized SMSO particle shed ~ $10^6$ nanoparticles into the solution (Supplementary Text).

Second, according to eq. (1), the BID model predicts a size-dependent dissolution rate, approaching zero for colloidal nanoparticles with sizes close to or smaller than $r^*$. To validate this dependence, we performed real-time confocal fluorescence microscopy to monitor the dissolution rate during the BID process (see Materials and Methods). A clear size-dependent dissolution rate was observed, with a decreasing size-reduction rate for smaller colloidal nanoparticles (Fig. 1F). To quantify the size-dependent dissolution rate, we applied a previously reported constant-composition (CC) technique (*25*) to extract the dissolution flux rate against time at different undersaturations determined by the pH of the solution (Fig. 1G&H; fig. S6&7; see Materials and Methods). The CC dissolution curves reached a plateau prior to complete dissolution, thus indicating the creation of metastable states both for undissolved large SMSO particles with roughened surfaces and colloidal nanoparticles shed into the solution.

Third, we hypothesized that in the same undersaturated solution, only nanoparticles with sizes $\leq r^*$ can be kinetically preserved, while bulk particles can still be dissolved (Fig. 1I). We experimentally verified that fresh, bulk SMSO particles were etched to nanoparticles in the same undersaturated solution despite a suppressed reaction for previously immersed particles (Fig. 1J, top). Furthermore, we found that SMSO colloidal nanoparticles produced in an undersaturated suspension resisted further dissolution after separation and re-immersion in a solution of the same undersaturation (Fig. 1J, bottom and fig. S8).

Lastly, we also verified minimal dissolution of bulk SMSO particles in pure water without citrate (pH = 7), thus confirming the importance of rationally designed undersaturated environments in the BID method (fig. S9). In summary, we have validated the kinetic preservation mechanism to produce stable colloidal solutions of SMSO nanophosphors via the BID approach.

**BID-produced SMSO colloids exhibit strong emission with a long luminescence lifetime**

We then characterized the luminescence properties of SMSO colloids prepared by the BID method (Fig. 2). The photoluminescence excitation and emission spectra of the SMSO colloid are identical to those of its corresponding bulk phosphor (Fig. 2A&B). In addition, the afterglow spectrum of the SMSO colloid agrees with that of its solid-state precursor (Fig. 2C). Lastly, the emission half-life of the SMSO colloid (~60 s) is similar to that of its corresponding bulk phosphor (~74 s; Fig. 2D). These results represent the first example of producing stable <50 nm colloids with a strong and persistent blue afterglow matching solid-state synthesized phosphors. Importantly, SMSO colloids produced from the BID method represent one of the brightest afterglow materials with blue emission and stable colloidal suspension in water (table S2), thus making it an ideal candidate to excite light-activated proteins *in vivo* without an external light source. Specifically, an absolute intensity measurement of an SMSO colloidal solution at 0.49 μM yields a photon emission rate of $5.25 \times 10^{11}$ p/s/cm$^2$/sr (Fig. 2E). Furthermore, the luminescence quantum yield of SMSO colloidal solution was measured to be ~21.0% (Materials and Methods), which is higher than that of photochemical afterglow systems as previously reported (*14*, *33*).

Next, we evaluated the long-term afterglow stability of SMSO colloids in water, phosphate-buffered saline (PBS), and fetal bovine serum (FBS). The SMSO colloid exhibits the same afterglow intensity in PBS in comparison to that in water, while its lower intensity in FBS is solely attributed to the absorption of FBS at 470 nm instead of chemical instability (Fig. 2F and fig. S10). Despite different environments, the SMSO colloid exhibits chronic stability in afterglow intensity over 14 days in water, PBS, and FBS at room temperature (Fig. 2G). Taken together, these characterizations reveal the BID method as a preferred approach to produce high-quality colloidal

solutions of nanophosphors that maintain the strong emission power of their bulk counterparts while significantly improving colloidal stability in water.

**The BID method is a generalizable approach for synthesizing colloidal solutions of nanophosphors spanning the visible spectrum**

The different activation spectra of light-responsive proteins require light sources of distinct wavelengths for efficient excitation. To this end, we apply the BID method to produce colloidal solutions of nanophosphors with afterglow wavelengths spanning the entire visible spectrum. Existing bottom-up approaches usually produce afterglow nanoparticles with red to near-infrared emission (table S2), thus prohibiting their use as light sources to excite common light-activatable proteins such as YFP, SSFO, and psCas9. In contrast, solid-state reactions offer a wide-range combination of host materials and activating ions to yield phosphors with a strong afterglow and tunable wavelengths, yet many of which remain refractory to wet chemical and mechanical milling methods with limited colloidal stability. For example, phosphors with strong persistent luminescence (*19*, *34*) and desirable phases (*35*) can only be produced at exceptionally high temperatures, while their color centers may be quenched by built-in stress and dislocations introduced during mechanical milling. We hypothesize that since most solid-state phosphors have low water solubility, eq. (2) predicts 10-100 nm nanoparticles produced via the BID process, thus offering a generalizable method to synthesize colloidal solutions of nanophosphors.

We rationally chose a select few persistent phosphors that can only be synthesized in solid-state reactions and exhibit strong afterglow spanning the visible spectrum to demonstrate the generalizability of the BID method. These selected phosphors have very low solubility in water and do not react with water (*36*–*38*), thus fulfilling the critical size requirement to apply the BID mechanism (eq. 1&2). Specifically, $Sr_4Al_{14}O_{25}$:Eu,Dy (SAO) exhibits strong afterglow at 490 nm and can only be synthesized at ≥1350 °C. In addition, wurtzite ZnS:Cu,Al and ZnS:Mn exhibit strong afterglow at 534 nm and 578 nm, respectively, and their specific polymorph can only be formed at ≥1000 °C. Moreover, $Ca_{0.85}Sr_{0.15}S$:Eu,Tm (CSS) represents one of the few materials with strong red afterglow at 650 nm and requires a high annealing temperature of 1100 °C (see Materials and Methods). The BID method successfully produced stable colloidal solutions of nanophosphors with emission colors consistent with their bulk precursors (Fig. 3A&B) and sizes below 100 nm (Fig. 3C-E). Furthermore, the afterglow spectra, afterglow kinetics, and XRD spectra of these nanophosphor colloids are all consistent with those of their bulk precursors (Fig. 3F&G; fig. S11). Taken together, these results confirm the BID method as a generalizable approach to synthesize stable nanophosphor colloids in water with their emission spectra spanning the entire visible spectrum (Fig. 3F; fig. S12&S13) while preserving their desirable polymorphs and afterglow properties.

**BID-produced colloids are among the brightest reported afterglow materials after delivery *in vivo***

We next sought to evaluate the afterglow intensity of BID-produced nanophosphor colloids after delivery *in vivo* and compare it to other reported afterglow materials. Unlike their bulk precursors, BID-produced nanophosphors exhibit superior colloidal stability, thus enabling them to be delivered via conventional administration routes and act as colloidal light sources. We selected two administration methods commonly used to deliver biocompatible colloidal solutions, subcutaneous and intravenous injection (*8*, *9*, *11*, *16*). We hypothesized that the strong afterglow of BID-produced colloids enabled ultrasensitive *in vivo* imaging by eliminating real-time excitation and tissue autofluorescence. As a result, the afterglow of *in vivo* administered nanophosphor colloids should

be detectable in deep tissue despite their much shorter wavelengths than other reported afterglow materials.

We subcutaneously injected all five colloidal solutions of persistent nanophosphors produced above (SMSO, SAO, ZnS:Cu,Al, ZnS:Mn, and CSS) and performed multicolor afterglow imaging (Fig. 4A). The distinct afterglow colors of these colloids allowed us to resolve their spatial distribution in live mice after delivery (Fig. 4B&C). Quantitative radiance measurements reveal strong emission intensity of all subcutaneously injected colloids despite attenuation through the skin (Fig. 4D). Strikingly, the mass-normalized afterglow intensity of the brightest BID-produced colloids is two orders of magnitude higher than the brightest afterglow nanomaterial reported to date in the same setting, regardless of emission wavelengths (table S2 and Fig. 4E). Importantly, the superiority of BID-produced nanophosphors is validated by comparing both subcutaneously injected materials *in vivo* and an aqueous solution of the material *ex vivo* (table S2). We attribute the brighter afterglow of BID-produced nanophosphors to their preservation of the optical properties of their bulk counterparts from solid-state reactions, which result in thermodynamically and kinetically more favorable formation of desirable polymorphs and point defects leading to stronger persistent luminescence. In addition, the exceptional afterglow intensity and minimal autofluorescence background enabled us to obtain a much higher signal-to-background ratio (SBR) up to 9,190× than that of fluorescence imaging (<23×) with the same injected colloids (Fig. 4F). Importantly, despite their unfavorably short emission wavelengths, the SBR values of BID-produced colloids even exceeded those obtained with red and NIR afterglow materials (table S2 and Fig. 4G).

Having demonstrated subcutaneous delivery of BID-produced nanophosphors, we next aimed to validate their feasibility as systemically delivered light sources via intravenous injection. Specifically, we injected the SMSO or SAO colloid solution, which was charged prior to injection (Fig. 4H and fig. S14), into the mouse tail vein. Immediately after injection, transcranial afterglow imaging through the intact skull reveals that intravenously administered colloids are spatially confined in cerebral vessels. Their afterglow was sufficiently bright to be visualized even through the intact skull despite their short wavelengths (470 nm and 490 nm for SMSO and SAO, respectively) (Fig. 4I&J). Line cross-sectional intensity analysis reveals spatially resolved cerebral vessels with similar widths to those imaged with fluorescence in the second near-infrared (NIR-II) window (Fig. 4K and fig. S15). These images represent the first example of transcranial afterglow imaging of cerebral vessels in the mouse brain.

Furthermore, the utility of BID-produced nanophosphors as systemically delivered light sources relies on their ability to be recharged during circulation *in vivo*. Previous demonstration of *in vivo* recharging of afterglow materials usually involved *in situ* recharging and activation at the same site for imaging (*8*, *17*, *39*). Despite the use of red or NIR light for recharging, the efficiency of recharging still remains limited, while recharging and imaging at the same location prohibits simultaneous afterglow imaging during recharging (*1*). We hypothesize that the intrinsic circulatory system of the animal can be leveraged to efficiently recharge intravenously-delivered BID-produced nanophosphors when they pass through superficial blood vessels, even with short-wavelength excitation light, at a different location in the body. To prove this hypothesis, we performed real-time afterglow imaging of the femoral artery in the mouse hindlimb, while applying remote periodic recharging of the circulating afterglow colloids in superficial hepatic vessels through noninvasive transdermal photoexcitation (Materials and Methods, fig. S16A&B). We found that the afterglow in the femoral artery increased after every recharging pulse, with a baseline intensity ~10× higher than that without recharging at 400 s after injection (fig. S16C). These results

represent the first demonstration of remote recharging of afterglow materials *in vivo* via the intrinsic circulatory system.

The three experiments of afterglow imaging above validated the remarkable afterglow intensity and rechargeability of BID-produced colloids in living mice. Compared to extensively reported afterglow nanoparticles in red and NIR spectra, BID-produced colloids benefit from their strong afterglow of blue-shifted photons, which may activate many blue-light-responsive proteins such as SSFO and psCas9 (Fig. 4E, Supplementary Text, and table S1) (*3*, *13*, *31*). The demonstrated compatibility with common administration routes, especially intravenous injection, provides a means to uniformly deliver these colloidal light sources throughout the body. To prove the biosafety of intravenously delivered colloidal light sources, we performed detailed biodistribution, secretion, and toxicology studies in mice and found minimal adverse effects to the subject after systemic administration of these colloids (fig. S17-19). These pharmacokinetics data suggest minimal retention of systemically delivered afterglow colloids at 1 week post administration. Nonetheless, multiple injections may be performed to facilitate their long-term utility in the same animal.

**BID-produced colloidal light sources enable internal excitation of genetically encoded fluorescent reporters with greater tissue penetration.**

The strong afterglow of BID-produced colloids in the blue spectrum allowed us to postulate their function as an intravital light source to excite light-responsive proteins endogenously expressed in the tissue. Specifically, genetically encoded fluorescent reporters, such as fluorescent proteins and their functional derivatives (e.g., GCaMP etc.), suffer from limited tissue penetration due to strong scattering and autofluorescence of their short excitation wavelengths. This disadvantage necessitates the invasive implantation of a cranial window or a gradient index (GRIN) lens (*40*) with limited field of view (FoV) and restrained behavior of the subject in a microscopic setup (*41*). In contrast, widefield afterglow imaging enables a much larger FoV and deeper tissue penetration by eliminating an external excitation, thus reducing scattering and autofluorescence. However, afterglow imaging has never been realized for endogenous fluorescent proteins. We hypothesized that systemically delivered colloidal light sources can enable widefield afterglow imaging of endogenously expressed fluorescent proteins with increased tissue penetration.

We set out to demonstrate widefield afterglow imaging of YFPs for the first time via BID-produced colloidal light sources. We delivered a colloidal solution of SMSO into the cerebral vessels of a transgenic mouse (B6.Cg-Tg(Thy1-YFP)16Jrs/J, YFP-16) expressing YFPs in neurons (Fig. 5A) (*42*). The spectral overlap between the afterglow spectrum of SMSO colloids and the excitation spectrum of YFP offers efficient excitation of YFP fluorescence by the afterglow of SMSO (fig. S20). We used widefield acquisition for whole-brain YFP imaging through the intact skull (Fig. 5B) to demonstrate a large FoV for potentially imaging free-behaving animals in future studies. When a traditional external excitation was applied, the excitation light was absorbed and scattered by the skull while producing autofluorescence (Fig. 5E). As a result, this process yielded epifluorescence images featuring skull structures that block YFP fluorescence from the underlying brain (Fig. 5F, right and fig. S21-22). Control experiments on wild-type (WT) mice without YFP expression revealed similar patterns in the epifluorescence images (Fig. 5F, left). Pearson correlation analysis between fluorescence images of WT vs YFP-16 mice reveals a high Pearson correlation coefficient of 0.93 (Fig. 5G, right and 5H), thus confirming the origin of these features arising from the skull rather than from the underlying brain (*43*). These observations confirmed the need to remove or thin the skull in conventional YFP imaging in the mouse brain (*40*).

In contrast to the external excitation, with an internal excitation enabled by systemically delivered colloidal light sources, YFP fluorescence was collected in the afterglow mode (Fig. 5C; see Materials and Methods). The resulting YFP afterglow image of the same mouse brain only revealed the spatial distribution of YFPs in the brain (i.e., in the brain parenchyma while excluding cerebral vessels) without any interference from the skull (Fig. 5D, right and fig. S21). Unlike epifluorescence imaging, afterglow images of WT vs YFP mouse brain exhibited dissimilar patterns (Fig. 5D). A low Pearson correlation coefficient of 0.20 suggests minimal feature colocalization between the WT vs YFP-16 mouse brain in the afterglow mode (Fig. 5G, left and 5H). These results demonstrate the unique ability of afterglow imaging to reveal deep-tissue features unresolvable by conventional fluorescence imaging with the intact skull. In summary, BID-produced colloidal light sources enabled widefield afterglow imaging of YFPs with minimal autofluorescence and scattering background from overlying tissues. Therefore, *in vivo* widefield afterglow imaging offers a much less invasive approach than conventional microscopy through a cranial window for imaging genetically encoded fluorescent reporters in the mouse brain.

## Discussion

Here, we report a generalizable method for producing stable colloidal solutions of nanophosphors from their solid-state bulk materials with exceptionally bright luminescence (up to $5.25 \times 10^{11}$ p/s/cm$^2$/sr), tunable emission wavelengths down to 470 nm, and small sizes (down to 20 nm). This method was enabled by the bioinspired demineralization (BID) process, which has been found in many biominerals such as tooth enamel and avian eggshells to afford exquisite control of complex nanostructures (*25*, *26*). Colloids produced by this approach exhibited the highest SBR for in-vivo imaging among reported materials, yielding the first example of transcranial afterglow imaging of cerebral vessels in the mouse brain. Owing to their strong emission intensity and colloidal stability in water, BID-produced colloidal light sources provide internal excitation of and enable afterglow imaging of genetically encoded fluorescent reporters in a mouse brain through the intact skull.

Compared to previously reported afterglow materials, the BID approach and BID-produced colloids have three unique advantages that enable their use as an internal light source. First, the BID approach can be applied to a wide range of solid-state phosphors to produce tunable emission down to 470 nm. These inorganic phosphors usually require specific polymorphs and dopant ions incompatible with conventional sol-gel synthesis and mechanical ball milling. As a result, the BID approach contrasts strongly with the limited range of conventional afterglow materials including $ZnGa_2O_4:Cr^{3+}$ (695 nm), semiconducting polymers (780 nm), and rare-earth doped $NaLnF_4$ nanoparticles (>1,000 nm) (*8*, *9*, *16*). Second, the BID approach preserves the crystallinity and emission intensity of solid-state phosphors in synthesized colloidal nanophosphors. This preservation is owing to a mild top-down process that produces the colloids, in strong contrast with harsh mechanical milling that usually yields mechanical and dislocation-induced quenching (*23*, *24*). Using the in-vivo intensity after subcutaneous injection as a metric for comparison, BID-produced colloids (~$3.8 \times 10^{10}$ p/s/cm$^2$/sr/(mg/mL), table S2) are two orders of magnitude higher than the brightest afterglow material reported previously (~$10^8$ p/s/cm$^2$/sr/(mg/mL), table S2). Furthermore, in an *ex vivo* solution, BID-produced colloids are five orders of magnitude brighter ($6.2 \times 10^{11}$ p/s/cm$^2$/sr/(mg/mL), table S2) than the brightest afterglow nanoparticles produced by other methods such as ball milling and grinding ($2 \times 10^6$ p/s/cm$^2$/sr/(mg/mL), table S2). The high quality of BID-produced colloids is also evidenced by remarkable stability over 1000 repeated recharging and emission cycles (fig. S23) and superior resistance against photobleaching even after prolonged exposure to strong excitation light (fig. S24), in contrast to rapid decay of organic afterglow materials (*9*, *11*). Third, the colloidal stability of BID-produced nanophosphors in water

yields sufficient biosafety for them to be used as systemically delivered light sources in live mice (Fig. 5). The demonstrated ability of transcranial afterglow imaging of YFPs thus offers a minimally invasive approach to image and modulate gene expression and neural activity in the mouse brain without any cranial windows or implanted GRIN lenses.

Furthermore, the BID method also enables unique opportunities for synthesizing stable colloidal suspensions of other functional materials for biomedical applications. Specifically, besides persistent phosphors, other functional materials that can only be synthesized via high-temperature solid-state reactions or annealing can also be processed via the BID method to yield stable colloidal suspensions in water. Many ceramic materials, such as mechanoluminescent ZnS (*44*), piezoelectric $LiTaO_3$ (*45*), and ferroelectric materials $LiNbO_3$ (*46*) can only be produced in the bulk and are thus insoluble in water. Nonetheless, we can leverage the same BID principle to produce corresponding stable colloids while preserving the structure and properties of their bulk counterparts for biological applications, such as *in vivo* fluorescence imaging (*41*), sono-optogenetics (*44*), ultrasound and magnetic neuromodulation (*47*), and flexible optoelectronics (*48*).

## Materials and Methods

**Chemicals.** Strontium carbonate ($SrCO_3$, ≥99.9%), silicon dioxide ($SiO_2$, 99.5%), boric acid ($H_3BO_3$, ≥99.5%), europium oxide ($Eu_2O_3$, 99.99%), dysprosium oxide ($Dy_2O_3$, 99.99%), magnesium carbonate hydroxide pentahydrate [$(MgCO_3)_4{\cdot}Mg(OH)_2{\cdot}5H_2O$, 99.5%], aluminum oxide ($Al_2O_3$, 99.99%), zinc sulfide (ZnS, 99.99%), copper (II) acetylacetonate (≥99.9%), manganese (II) carbonate ($MnCO_3$, ≥99.9%), sulfur (99.98%), calcium carbonate ($CaCO_3$, ≥99.95%), thulium (III) acetate hydrate (99.9%), sodium citrate dihydrate (≥99%), strontium chloride ($SrCl_2$, ≥99.99%), magnesium chloride ($MgCl_2$, 99.9%), and citric acid (≥99.5%) were purchased from Sigma-Aldrich Inc. Ethanol, fetal bovine serum (FBS), hydrochloric acid, nitric acid ($HNO_3$), 1× phosphate-buffered saline (PBS), paraformaldehyde, and N,N-dimethylformamide (DMF) were purchased from Thermo Fisher Scientific. Methoxy(polyethylene glycol)-silane (mPEG-silane, 20 kDa) was purchased from Jenkem Technology. All chemicals were used as purchased.

**Synthesis of $Sr_2MgSi_2O_7$:Eu,Dy (SMSO) bulk phosphor and colloidal nanophosphor.** SMSO nanophosphor colloid was prepared by a two-step method. First, SMSO bulk phosphor was synthesized via a high temperature solid-state chemical reaction. In this reaction, 1166.28 mg of $SrCO_3$ (7.9 mmol), 388.52 mg of $(MgCO_3)_4{\cdot}Mg(OH)_2{\cdot}5H_2O$ (0.8 mmol), 480.64 mg of $SiO_2$ (8 mmol), 4.2 mg of $Eu_2O_3$ (0.012 mmol), 14.92 mg of $Dy_2O_3$ (0.04 mmol), and 14.83 mg of $H_3BO_3$ (0.24 mmol) were added into an agate mortar and then ground by a pestle for 1 h. Then the mixed precursors were annealed at 1050 °C for 2 h under a reduction atmosphere of 5% $H_2$ in Ar. After cooling to room temperature, the as-prepared SMSO bulk materials were ball-milled using zirconia beads in a high energy ball mill (8000D Mixer/Mill, SPEX SamplePrep, Metuchen, NJ) for 30 min. In the second step, sodium citrate buffer (0.08 mol/L, pH=6) was prepared as the bioinspired demineralization (BID) solution. Subsequently, the ball-milled SMSO particles (200 mg) and 24 mL of sodium citrate buffer were added into a flask and stirred at 80 °C for 72 h, during which the pH of the solution quickly increased to and stabilized at ~10. Final SMSO nanophosphor colloid was obtained by centrifugation at 1000 rpm (Sorvall Legend X1R Centrifuge; Thermo Fisher Scientific, Waltham, MA) for 10 min to remove large parent particles.

**Synthesis of $Sr_4Al_{14}O_{25}$:Eu,Dy (SAO) bulk phosphor and colloidal nanophosphor.** SAO bulk phosphor was prepared by a conventional solid-state reaction. 1476 mg of $SrCO_3$ (10 mmol), 1784 mg of $Al_2O_3$ (17.5 mmol), 26 mg of $Eu_2O_3$ (0.075 mmol), and 46 mg of $Dy_2O_3$ (0.125 mmol) were weighed and thoroughly ground in an agate mortar for 1 h. The mixed powder was annealed at 1350

°C for 2 h under the reduction atmosphere of 5% $H_2$ in Ar. After cooling to room temperature, the prepared SAO bulk powder was milled using zirconia beads in a high energy ball mill for 30 min. The same BID procedure as in the preparation of the SMSO colloid was followed to synthesize the SAO colloid.

**Synthesis of ZnS:Cu,Al bulk phosphor and colloidal nanophosphor.** ZnS:Cu,Al bulk phosphor was prepared by a conventional solid-state reaction. First, 2.62 mg of copper acetylacetonate (0.01 mmol) was dissolved in 1 mL of chloroform to prepare a copper precursor solution (0.01 mol/L). Subsequently, 0.98 g of ZnS (10 mmol) and 3 mg of $Al_2O_3$ (0.03 mmol) were weighed and put into an agate mortar. Meanwhile, 10 μL of the copper precursor solution and 6 mg of $H_3BO_3$ as the flux were added into the agate mortar and thoroughly ground for 1 h. Lastly, the mixed powder was annealed at 1100 °C for 2 h under a reduction atmosphere of 5% $H_2$ in Ar. After cooling to room temperature, the prepared ZnS:Cu,Al powder was ball-milled using zirconia beads in a high energy ball mill for 30 min. The same BID procedure as in the preparation of the SMSO colloid was followed to synthesize the ZnS:Cu,Al colloid.

**Synthesis of ZnS:Mn bulk phosphor and colloidal nanophosphor.** ZnS:Mn bulk phosphor was prepared by a conventional solid-state reaction. 0.98 g of ZnS (10 mmol), 1.15 mg of $MnCO_3$ (0.01 mmol), and 6 mg of $H_3BO_3$ as the flux were weighed and ground in an agate mortar for 1 h. The mixed powder was then annealed at 1100 °C for 2 h under a reduction atmosphere of 5% $H_2$ in Ar. After cooling to room temperature, the prepared ZnS:Mn powder was ball-milled using zirconia beads in a high energy ball mill for 30 min. The same BID procedure as in the preparation of the SMSO colloid was followed to synthesize the ZnS:Mn colloid.

**Synthesis of $Ca_{0.85}Sr_{0.15}S$:Eu,Tm (CSS) phosphor and colloidal nanophosphor.** CSS bulk phosphor was prepared by a conventional solid-state reaction. 1 g of $CaCO_3$ (10 mmol), 250 mg of $SrCO_3$ (1.7 mmol), 0.7 mg of $Eu_2O_3$ (0.004 mmol), 4.8 mg of thulium (III) acetate hydrate (0.014 mmol), and 6 mg of $H_3BO_3$ (0.1 mmol) as the flux were weighed and ground in an agate mortar for 1 h. Then, 1283 mg of sulfur (40 mmol) was added into the mixed powder and annealed at 1100 °C for 1 h using activated charcoal to provide a reducing atmosphere. After cooling to room temperature, the prepared CSS powder was ball-milled using zirconia beads in a high energy ball mill for 30 min. Subsequently, the ball-milled CSS particles (200 mg) and 24 mL of the BID solution were added into a flask and stirred at room temperature for 2 h. Final CSS colloid was obtained by centrifugation at 1000 rpm (Sorvall Legend X1R Centrifuge; Thermo Fisher Scientific, Waltham, MA) for 10 min to remove large parent particles.

**Surface functionalization of nanophosphor colloids.** For *in vivo* applications, the as-prepared colloids were functionalized with mPEG-silane (20 kDa). First, the SMSO colloid was transferred into a cellulose dialysis tubing (MWCO = 30 kDa) and dialyzed against water for 2 days to remove excess citrate ions. Subsequently, surface hydroxylation was performed on the surface of the SMSO colloid. Specifically, a 20 μL solution of sodium hydroxide (10 mol/L) was added into 10 mL of SMSO colloid (67 nmol/L) and sonicated for 1 h at room temperature (*49*). After surface hydroxylation, the SMSO colloid was washed with water and anhydrous DMF three times in each solvent and dispersed in DMF. Finally, 40 mg of mPEG-silane (20 kDa) was added into 10 mL of the SMSO DMF solution and sonicated at 50 °C for 4 h. The PEGylated-SMSO colloid was washed with pure DMF and water three times in each solvent and then dispersed in PBS for *in vivo* experiments. The same PEGylation procedure was followed to prepare the solutions containing SAO, ZnS:Cu,Al, ZnS:Mn, and CSS colloids.

**Characterizations.** X-ray diffraction (XRD) patterns were acquired by using a diffractometer (PANalytical Empyrean, Malvern Panalytical Ltd., Malvern, United Kingdom) with Cu Kα ($\lambda$ = 1.540598 Å) radiation at a 45 kV tube voltage and a 40 mA tube current. The transmission electron microscope (TEM) images of the samples were captured on a Field Electron and Ion Company

Tecnai TEM (FEI Company, Hillsboro, Oregon) equipped with a charge-coupled device (CCD) camera. Scanning electron microscope (SEM) images were recorded by an Apreo S LoVac SEM (Thermo Fisher Scientific, Waltham, MA). Fourier transform infrared (FTIR) spectroscopy was performed using a Nicolet iS50 FT/IR spectrometer (Thermo Fisher Scientific, Waltham, MA) on dried powder samples. Absorption spectra were measured by an Evolution 350 UV-Vis Spectrophotometer (Thermo Fisher Scientific, Waltham, MA). For the UV-Vis measurement of the silica-citrate complex, a Savitzky-Golay filter with a window size of 10 is applied due to its low absorption. All other UV-Vis absorption spectra are displayed as is. Photoluminescence spectra of all samples were measured by a Horiba FluoroLog Fluorometer spectrophotometer (HORIBA Ltd., Kyoto, Japan) in a 1-cm quartz cuvette. In photoluminescence measurements, the excitation wavelength was 380 nm and the measured range of photoluminescence was 400-700 nm. Elemental analyses of the samples were characterized by an inductively coupled plasma mass spectrometer (ICP-MS, Thermo Scientific X-SERIES II Quadrupole, Thermo Fisher Scientific, Waltham, MA). Nuclear magnetic resonance (NMR) spectra were collected on a 500 MHz Varian Inova NMR spectrometer (Varian, Inc., Palo Alto, CA). The Brunauer-Emmett-Teller (BET) isotherm was measured using a surface area and pore size analyzer (Anton-Paar NovaTouch, Boynton Beach, FL).

**Determining molar concentrations of nanophosphor colloids.** The molar concentration of each colloid was calculated with the Beer-Lambert Law ($A=\mathcal{E}lc$), in which $A$ is the absorbance, $\mathcal{E}$ is the extinction coefficient per mole of colloidal nanoparticles per liter (L/mol/cm), $l$ is the optical path length (cm), and $c$ is the molar concentration (mol/L) of the colloidal nanoparticles of the same sample. Specifically, $\mathcal{E}$ was determined by linear fitting of the measured absorbance at 400 nm for a specific colloid at three concentrations against their concentrations determined by ICP-MS measurements.

**Real-time confocal fluorescence microscopy of the BID process.** The BID process of SMSO particles in the sodium citrate buffer was characterized with real-time fluorescence imaging, which was performed on a LSM 980 confocal microscope (Carl Zessis, Oberkochen, Germany) using a 63× oil-immersion Plan-APO objective (numerical aperture: 1.4) with an excitation wavelength of 405 nm and an exposure time of 1.62 s per image. The filter set consisted of an excitation filter at 405 nm, a beam splitter at 435 nm, and an emission filter at 465 nm. A z-stack of 31 slices with an interval of 0.38 μm (pinhole size: 1.83 airy unit) was acquired per time frame to account for the vertical drifting of SMSO particles.

**The constant-composition (CC) technique.** Dissolution experiments with the CC technique were performed by following previously reported protocols (*25*, *27*). Specifically, all reactions were carried out in magnetically stirred three-neck round-bottom flasks. Undersaturated reaction solutions (60 mL) were prepared by mixing 360 μL of $SrCl_2$ (1 mol/L) and 180 μL of $MgCl_2$ (1 mol/L) solutions with the sodium citrate buffer (0.08 mol/L) such that $[Mg^{2+}] = 3$ mmol/L and $[Sr^{2+}] = 6$ mmol/L. The pH was adjusted to the desired value with either hydrochloric acid (12.1 mol/L) or sodium hydroxide (10 mol/L). The undersaturated solution was then heated and kept at 90 °C in a silicon oil bath during the reaction. The CC dissolution reaction was initiated by introducing bulk SMSO particles (100 mg) with a specific surface area of 43,850 $cm^2/g$ (fig. S6). During the reaction, the pH of the solution was constantly monitored using a benchtop pH meter (SevenCompact S230; Mettler Toledo, Greifensee, Switzerland), which provided feedback control for the titrant (0.08 mol/L citrate buffer pH = 1.75) to keep the pH within ± 0.1 of the desired value. The composition and concentration of the titrant were calculated to ensure $[MgCit^-]$, $[SrCit^-]$, $[HCit^{2-}]$, and $[Cit^{3-}]$ all stayed constant during the dissolution reaction if the pH remained constant according to the equation in fig. S1. Due to the unknown stoichiometry of the silica-citrate complex, we did not

control its concentration at a constant, and we argue that the potential formation of silica clusters contributes a unity activity (e.g., independent of its concentration) to the chemical equilibrium.

**Proving kinetically preserved dissolution to produce nanophosphor colloids.** In this kinetically preserved dissolution experiment, 1000 mg of ball-milled SMSO particles and 120 mL of sodium citrate buffer (0.08 mol/L, pH=6) were added into a flask and stirred at 80 °C for 10 min. Then, the SMSO suspension was centrifuged at 1000 rpm for 10 min to remove large parent particles and at 8000 rpm for 20 min to separate nanoparticles. The supernatant, which contained an undersaturated solution for SMSO, was collected and equally divided into two parts: Solution 1 was added with the SMSO nanophosphor colloid and kept stirring at 80 °C for 3 days. A bright field image, an image showing the Tyndall effect with a 632.8 nm HeNe laser beam (ThorLabs), and an afterglow image were taken at day 0 and day 3 for this mixture (Fig. 1J, bottom row). Meanwhile, the UV-vis spectrum of this mixture was measured at day 0 and day 3 (fig. S8). Solution 2 was added with SMSO bulk precursor particles and kept stirring at 80 °C for 3 days. The same images were taken at day 0 for the mixture of Solution 2 and at day 3 for the mixture of Solution 2 after passing 1000 rpm for 10 min (Fig. 1J, top row).

**Spectral characterizations of persistent luminescence.** Persistent luminescence spectra of bulk phosphors and colloidal nanophosphors were acquired using a fiber-coupled spectrometer (OCEAN-HDX-VIS-NIR; Ocean Optics, Orlando, FL) that measures the whole spectrum in the range of 350-900 nm spontaneously. A polydimethylsiloxane (PDMS) phantom containing a specific phosphor or nanophosphor colloid was used as the sample for spectral characterizations. Specifically, the PDMS phantom was charged by a 365-nm light emitting diode (LED; SOLIS-365C, Thorlabs, Newton, NJ) at 5.7 mW/mm$^2$ for 10 s. The persistent luminescence spectrum was acquired immediately after the charging light was turned off. Averaging over multiple measurements was applied as needed to reduce the noise of the spectrum.

**Time-resolved intensity measurements of persistent luminescence.** PDMS phantoms as prepared above were charged for 10 s by a 365-nm LED at 0.13 mW/mm$^2$, and a photomultiplier tube (PMT1001; Thorlabs, Newton, NJ) was put in the close vicinity of the phantom to collect the persistent luminescence after the charging light was turned off. The output voltage from the PMT, which exhibits a linear dependence on light intensity, was then collected by a multifunction input/output (I/O) device (NI USB-6221, National Instruments, Austin, TX).

**Luminescence quantum yield measurement.** The luminescence quantum yield measurement was conducted by following protocols established in previous reports (*14*, *33*, *50*). Specifically, the SMSO nanophosphor colloid was excited by a collimated 365-nm light beam coupled from an LED (M365LP1, Thorlabs, Newton, NJ). An integrating sphere (IS200, Thorlabs, Newton, NJ) and a non-scanning fiber-coupled spectrometer (OCEAN-HDX-VIS-NIR; Ocean Optics, Orlando, FL) were used to redirect and collect the excitation and emission light simultaneously both during and after the recharging. The absorbed photons were measured by replacing the SMSO colloid with water and repeating the above procedure. The luminescence quantum yield was then calculated as follows:

$$QY = \frac{Photons\ emitted}{Photons\ absorbed} = \frac{\int_0^{t_{Lum}} I_{Em}\, dt}{(I_{Ex\_ref} - I_{Ex\_SMSO})\, t_{Ex}}$$

where QY is the luminescence quantum yield; $I_{Em}$ is the emission light intensity; $I_{Ex\_ref}$ and $I_{Ex\_SMSO}$ are the excitation light intensity in the presence of water or SMSO nanophosphor colloid, respectively; $t_{Lum}$ and $t_{Ex}$ are the duration of luminescence and excitation light, respectively.

**Repetitive recharging stability assessment.** PDMS phantoms as prepared above were charged by a 365-nm LED at 1 mW/mm$^2$ for 100-ms, followed by image acquisition using a scientific CMOS camera (CS165MU, Thorlabs, Newton, NJ) with 1-Hz frame rate for 5 frames, resulting in a

recharging duty cycle of 2%. The same recharging and image acquisition cycle was repeated for 1000 times to assess the repetitive recharging stability of BID-produced nanophosphor.

**Photobleaching resistance assessment.** PDMS phantoms as prepared above were charged by a 365-nm LED at 1 mW/mm$^2$ for 100-ms, followed by image acquisition using a scientific CMOS camera. Afterwards, the phantoms were bleached by 1 mW/mm$^2$ for 24 hr continuously. Then the same recharging and image acquisition procedure was repeated, and the afterglow intensities of the phantoms were normalized against those before photobleaching.

**Vertebrate animal subjects.** Adult (20-30 g) BALB/cJ mice (male, 8 weeks old, Jackson Laboratory, Bar Harbor, ME), J:Nu nude mice (male, 6 weeks old, Jackson Laboratory, Bar Harbor, ME), C57BL/6J mice (male, 6 weeks old, Jackson Laboratory, Bar Harbor, ME), and B6.Cg-Tg(Thy1-YFP)16Jrs/J mice (male, 6 weeks old, Jackson Laboratory, Bar Harbor, ME) were the vertebrate animal subjects used in this study. All procedures performed on mice were approved by Stanford University's Administrative Panel on Laboratory Animal Care (APLAC). The animal care and use programs at Stanford University meet the requirements of all federal and state regulations governing the humane care and use of laboratory animals, including the USDA Animal Welfare Act, and PHS Policy on Humane Care and Use of Laboratory Animals. The laboratory animal care program at Stanford is accredited by the Association for the Assessment and Accreditation of Laboratory Animal Care (AAALAC International). Animals were group-housed on a 12 h: 12 h light: dark cycle in the Stanford University's Veterinary Service Center (VSC) and fed with food and water ad libitum as appropriate.

**Persistent luminescence imaging of subcutaneously injected nanophosphor colloids.** Nude mice were anesthetized by intraperitoneal injection of 80 mg/kg ketamine (KetaVed®, Vedco, Inc., St. Joseph, MO) and 1 mg/kg dexdomitor (Dexmedesed™, Dechra Veterinary Products, Overland Park, KS). To maintain the body temperature and prevent hypothermia, a homeothermic blanket (Harvard Apparatus, Holliston, MA) was set to 37 °C and placed underneath the anesthetized mouse. A blackout fabric (BK5; Thorlabs, Newton, NJ) was put underneath the mice to reduce the background reflection when taking the image. 50 μL of colloidal solutions (SMSO, 146 nmol/L; SAO, 4 nmol/L; ZnS:Cu,Al, 80 nmol/L; ZnS:Mn, 31 nmol/L; CSS, 81 nmol/L) were then injected subcutaneously at five different locations under the dorsal skin as indicated by Fig. 4A. The colloids were then charged by a 365-nm LED at 0.5 mW/mm$^2$ for 5 s before image acquisition. Color images in Fig. 4C were acquired using the above-mentioned color digital camera with an ISO of 12800 and an exposure time of 10 s. The image in Fig. 4D was acquired using an IVIS Spectrum small animal imaging system (Spectral Instruments Imaging; Tucson, AZ) with an exposure time of 0.5 s at 10 s after the cease of the charging light.

**Persistent luminescence brain vascular imaging.** BALB/cJ mice were anesthetized using the above-mentioned ketamine/dexdomitor cocktail, and placed on the homeothermic blanket set to 37 °C. Hair removal lotion (Nair®, Church & Dwight, Ewing, NJ) was used for depilation of the mouse head, and iodophor was applied to sterilize the depilated scalp skin. Incision and its elongation were made by surgical scissors to expose the cranial bone. The blackout fabric was placed underneath the mouse as mentioned above. 200 μL of pre-charged nanophosphor colloids dispersed in 1× PBS (SMSO, 493 nmol/L; SAO, 8 nmol/L) were then delivered into the bloodstream through tail-vein injection, and the persistent luminescence image was acquired immediately after the injection using an electron-multiplying CCD (EMCCD, iXon Ultra 888, Andor Technology, Belfast, United Kingdom) with a 30 s exposure time.

**Remote recharging and afterglow imaging of the femoral artery.** Nude mice were anesthetized using the above-mentioned ketamine/dexdomitor cocktail, and placed on the homeothermic blanket set to 37 °C. Incision and its elongation on the hindlimb skin were made by surgical scissors to expose the femoral artery. The blackout fabric was placed underneath the mouse as mentioned

above. 200 μL of pre-charged nanophosphor colloids dispersed in 1× PBS (SAO, 8 nmol/L) were then injected intravenously. 5 s after the injection, 15 frames of afterglow images (~ 31.5 s in total) were acquired without recharging using the EMCCD with 2 s exposure time and 0.1 s interframe latency. Subsequently, a collimated 365-nm light beam (1 $mW/mm^2$) coupled from a LED was turned on for 2 s to recharge the circulating nanophosphors in the hepatic vessels in the liver region. 10 frames of afterglow images (~ 21 s in total) were acquired using the EMCCD with the same imaging parameters following each recharging pulse. This remote recharging and afterglow imaging cycle was repeated for 10 periods. See fig. S16A for more information.

**Afterglow imaging of YFPs in the mouse brain.** After delivery of an SMSO colloidal solution (493 nmol/L), the scalp was removed to expose the skull, and the SMSO colloid in the brain blood vessels was charged by a 365-nm LED at 0.5 $mW/mm^2$ for 5 s before image acquisition using the EMCCD with 30 s exposure time. Two afterglow images were collected using a 482-nm bandpass (482 BP) filter and a 550-nm longpass (550 LP) filter, respectively. To account for the spatial variation of the light source inside blood vessels and get the YFP afterglow images in Fig. 5D, we subtracted the background of the 550 LP and 482 BP images and then performed flat-field correction by normalizing the 550 LP image against the 482 BP image.

***In vivo* biodistribution study.** ICP-MS was used to study the biodistribution of systemically delivered SMSO colloids *in vivo*. Six BALB/cJ mice intravenously injected with 200 μL of SMSO colloid dispersed in 1× PBS (493 nmol/L) were divided into two groups (n = 3 for each group). Then the two groups of mice were sacrificed at 24 h and 168 h post-injection, respectively, and main organs including the heart, liver, spleen, lung, kidneys, and brain were collected. Organs were weighed and dissolved in 35% $HNO_3$ at 70 °C overnight. The digested $HNO_3$ solutions were diluted 20 times by water and measured by ICP-MS. The percent injected dose per gram of tissue (%ID/gram) in each organ was obtained by normalizing the amount of nanophosphors retained in the organ against both the initial injected dose and the organ mass.

**Histological study of potential tissue damage after colloid injection.** Three BALB/cJ mice intravenously injected with 200 μL of SMSO colloids dispersed in 1× PBS (493 nmol/L) were sacrificed at 30 days post-injection. In addition, three uninjected mice were sacrificed as the control group. Major organs (brain, heart, liver, spleen, lungs, and kidneys) were harvested and fixed in 4% paraformaldehyde. After 48 h fixation, these organs were embedded in paraffin, followed by sectioning at 10 μm slices. These organ slices were stained with hematoxylin and eosin (H&E) and imaged using a microscope (Leica DM2700 M, Wetzlar, Germany).

**Metabolic study for quantifying excretion of injected nanophosphor colloids**. Three BALB/cJ mice were individually housed in a metabolic cage after being intravenously injected with 200 μL of SMSO colloids dispersed in 1× PBS (493 nmol/L). Feces and urine samples were collected over 7 days. These samples were weighed and dissolved in 35% $HNO_3$ at 70 °C overnight and then measured by ICP-MS. The %ID/gram value in each sample was obtained by normalizing the amount of nanophosphors detected in the sample against both the initial injected dose and the excreta mass.

**Statistical analysis.** The variance in SBR of afterglow or fluorescence imaging (Fig. 4F) and Pearson's correlation coefficients of WT and YFP-16 afterglow or fluorescence images (Fig. 5H) was calculated, by which the pooled standard deviation (SD) among each experimental group was determined. Comparisons between experimental groups were made using one-way analysis of variance (ANOVA) without normality assumption given its reasonable tolerance of violations to normal distribution (*51*). *P* values of less than 0.05 were considered statistically significant. The values of *N*, *F* and *P* are provided in the figure captions.

## References


1. G. Hong, A. L. Antaris, H. Dai, Near-infrared fluorophores for biomedical imaging. *Nature Biomedical Engineering* **1,** 0010 (2017).

2. L. Fenno, O. Yizhar, K. Deisseroth, The development and application of optogenetics. *Annu. Rev. Neurosci.* **34**, 389–412 (2011).

3. Y. Nihongaki, F. Kawano, T. Nakajima, M. Sato, Photoactivatable CRISPR-Cas9 for optogenetic genome editing. *Nat. Biotechnol.* **33**, 755–760 (2015).

4. Z. Huang, Y. Wu, M. E. Allen, Y. Pan, P. Kyriakakis, S. Lu, Y.-J. Chang, X. Wang, S. Chien, Y. Wang, Engineering light-controllable CAR T cells for cancer immunotherapy. *Sci Adv*. **6**, eaay9209 (2020).

5. S. H. Yun, S. J. J. Kwok, Light in diagnosis, therapy and surgery. *Nat Biomed Eng*. **1** (2017), doi:10.1038/s41551-016-0008.

6. Y. Yang, M. Wu, A. J. Wegener, A. Vázquez-Guardado, A. I. Efimov, F. Lie, T. Wang, Y. Ma, A. Banks, Z. Li, Z. Xie, Y. Huang, C. H. Good, Y. Kozorovitskiy, J. A. Rogers, Preparation and use of wireless reprogrammable multilateral optogenetic devices for behavioral neuroscience. *Nat. Protoc.* **17**, 1073–1096 (2022).

7. A. D. Mickle, S. M. Won, K. N. Noh, J. Yoon, K. W. Meacham, Y. Xue, L. A. McIlvried, B. A. Copits, V. K. Samineni, K. E. Crawford, K. Do Hoon, P. Srivastava, B. H. Kim, S. Min, Y. Shiuan, Y. Yun, M. A. Payne, J. Zhang, H. Jang, Y. Li, H. Henry Lai, Y. Huang, S.-I. Park, R. W. Gereau, J. A. Rogers, A wireless closed-loop system for optogenetic peripheral neuromodulation. *Nature*. **565** (2019), pp. 361–365.

8. T. Maldiney, A. Bessière, J. Seguin, E. Teston, S. K. Sharma, B. Viana, A. J. J. Bos, P. Dorenbos, M. Bessodes, D. Gourier, D. Scherman, C. Richard, The in vivo activation of persistent nanophosphors for optical imaging of vascularization, tumours and grafted cells. *Nat. Mater.* **13**, 418–426 (2014).

9. Q. Miao, C. Xie, X. Zhen, Y. Lyu, H. Duan, X. Liu, J. V. Jokerst, K. Pu, Molecular afterglow imaging with bright, biodegradable polymer nanoparticles. *Nat. Biotechnol.* **35**, 1102–1110 (2017).

10. Z. Li, Y. Zhao, K. Huang, L. Huang, Y. Zhang, H. Yang, G. Han, Enhancing Rechargeable Persistent Luminescence via Organic Dye Sensitization. *Angew. Chem. Int. Ed Engl.* **60**, 15886–15890 (2021).

11. Y. Jiang, J. Huang, X. Zhen, Z. Zeng, J. Li, C. Xie, Q. Miao, J. Chen, P. Chen, K. Pu, A generic approach towards afterglow luminescent nanoparticles for ultrasensitive in vivo imaging. *Nat. Commun.* **10**, 2064 (2019).

12. R. N. Day, M. W. Davidson, The fluorescent protein palette: tools for cellular imaging. *Chem. Soc. Rev.* **38**, 2887–2921 (2009).

13. X. X. Zhou, X. Zou, H. K. Chung, Y. Gao, Y. Liu, L. S. Qi, M. Z. Lin, A Single-Chain

Photoswitchable CRISPR-Cas9 Architecture for Light-Inducible Gene Editing and Transcription. *ACS Chemical Biology*. **13** (2018), pp. 443–448.

14. X. Su, X. Kong, K. Sun, Q. Liu, Y. Pei, D. Hu, M. Xu, W. Feng, F. Li, Enhanced Blue Afterglow through Molecular Fusion for Bio-applications. *Angew. Chem. Int. Ed Engl.*, e202201630 (2022).

15. L. Ma, X. Zou, M. Hossu, W. Chen, Synthesis of ZnS:Ag,Co water-soluble blue afterglow nanoparticles and application in photodynamic activation. *Nanotechnology*. **27**, 315602 (2016).

16. P. Pei, Y. Chen, C. Sun, Y. Fan, Y. Yang, X. Liu, L. Lu, M. Zhao, H. Zhang, D. Zhao, X. Liu, F. Zhang, X-ray-activated persistent luminescence nanomaterials for NIR-II imaging. *Nat. Nanotechnol.* (2021), doi:10.1038/s41565-021-00922-3.

17. Z. Li, Y. Zhang, X. Wu, L. Huang, D. Li, W. Fan, G. Han, Direct Aqueous-Phase Synthesis of Sub-10 nm "Luminous Pearls" with Enhanced in Vivo Renewable Near-Infrared Persistent Luminescence. *J. Am. Chem. Soc.* **137**, 5304–5307 (2015).

18. Q. L. M. De Chermont, C. Chanéac, J. Seguin, F. Pellé, S. Maîtrejean, J.-P. Jolivet, D. Gourier, M. Bessodes, D. Scherman, Nanoprobes with near-infrared persistent luminescence for in vivo imaging. *Proceedings of the National Academy of Sciences*. **104**, 9266–9271 (2007).

19. F. Liu, W. Yan, Y.-J. Chuang, Z. Zhen, J. Xie, Z. Pan, Photostimulated near-infrared persistent luminescence as a new optical read-out from Cr3 -doped LiGa5O8. *Scientific Reports*. **3** (2013), , doi:10.1038/srep01554.

20. Y. Li, M. Gecevicius, J. Qiu, Long persistent phosphors—from fundamentals to applications. *Chem. Soc. Rev.* **45**, 2090–2136 (2016).

21. P. F. Smet, K. Van den Eeckhout, O. Q. De Clercq, D. Poelman, Persistent Phosphors. *Including Actinides* (2015), pp. 1–108.

22. C. Suryanarayana, Mechanical alloying and milling. *Prog. Mater Sci.* **46**, 1–184 (2001).

23. D. Tu, C.-N. Xu, Y. Fujio, S. Kamimura, Y. Sakata, N. Ueno, Phosphorescence quenching by mechanical stimulus in CaZnOS:Cu. *Applied Physics Letters*. **105** (2014), p. 011908.

24. X. Qin, X. Liu, W. Huang, M. Bettinelli, X. Liu, Lanthanide-Activated Phosphors Based on 4f-5d Optical Transitions: Theoretical and Experimental Aspects. *Chem. Rev.* **117**, 4488–4527 (2017).

25. R. Tang, L. Wang, C. A. Orme, T. Bonstein, P. J. Bush, G. H. Nancollas, Dissolution at the Nanoscale: Self-Preservation of Biominerals. *Angewandte Chemie*. **116** (2004), pp. 2751–2755.

26. D. Athanasiadou, W. Jiang, D. Goldbaum, A. Saleem, K. Basu, M. S. Pacella, C. F. Böhm, R. R. Chromik, M. T. Hincke, A. B. Rodríguez-Navarro, H. Vali, S. E. Wolf, J. J. Gray, K. H. Bui, M. D. McKee, Nanostructure, osteopontin, and mechanical properties of calcitic

779 avian eggshell. *Sci Adv*. **4**, eaar3219 (2018).

780 27. R. Tang, G. H. Nancollas, C. A. Orme, Mechanism of dissolution of sparingly soluble
781 electrolytes. *J. Am. Chem. Soc.* **123**, 5437–5443 (2001).

782 28. P. M. Dove, N. Han, J. J. De Yoreo, Mechanisms of classical crystal growth theory explain
783 quartz and silicate dissolution behavior. *Proc. Natl. Acad. Sci. U. S. A.* **102**, 15357–15362
784 (2005).

785 29. L. Ratke, P. W. Voorhees, *Growth and Coarsening: Ostwald Ripening in Material*
786 *Processing* (Springer Science & Business Media, 2013).

787 30. W. Wu, G. H. Nancollas, Determination of interfacial tension from crystallization and
788 dissolution data: a comparison with other methods. *Adv. Colloid Interface Sci.* **79**, 229–279
789 (1999).

790 31. E. S. Boyden, F. Zhang, E. Bamberg, G. Nagel, K. Deisseroth, Millisecond-timescale,
791 genetically targeted optical control of neural activity. *Nat. Neurosci.* **8**, 1263–1268 (2005).

792 32. I. P. Sahu, D. P. Bisen, N. Brahme, R. Sharma, Luminescence properties of Eu2 , Dy3 -
793 doped Sr2MgSi2O7, and Ca2MgSi2O7 phosphors by solid-state reaction method. *Research*
794 *on Chemical Intermediates*. **41** (2015), pp. 6649–6664.

795 33. Q. Zhou, M. Xu, W. Feng, F. Li, Quantum Yield Measurements of Photochemical Reaction-
796 Based Afterglow Luminescence Materials. *J. Phys. Chem. Lett.* **12**, 9455–9462 (2021).

797 34. Y. Gao, R. Li, W. Zheng, X. Shang, J. Wei, M. Zhang, J. Xu, W. You, Z. Chen, X. Chen,
798 Broadband NIR photostimulated luminescence nanoprobes based on CaS:Eu 2+ ,Sm 3+
799 nanocrystals. *Chem. Sci.* **10**, 5452–5460 (2019).

800 35. Y. Lin, Z. Tang, Z. Zhang, C. W. Nan, Anomalous luminescence in Sr4Al14O25:Eu, Dy
801 phosphors. *Appl. Phys. Lett.* **81**, 996–998 (2002).

802 36. H. Li, S. Yin, Y. Wang, T. Sekino, S. W. Lee, T. Sato, Green phosphorescence-assisted
803 degradation of rhodamine Bdyes by Ag3PO4. *J. Mater. Chem. A Mater. Energy Sustain.* **1**,
804 1123–1126 (2013).

805 37. C. Zhang, M. Zhang, W. Zheng, J. Wei, S. Wang, P. Huang, X. Cheng, T. Dai, Z. Chen, X.
806 Chen, A new class of luminescent nanoprobes based on main-group Sb3+ emitters. *Nano*
807 *Res.* **15**, 179–185 (2022).

808 38. J. Wang, Y. Zhu, C. A. Grimes, Q. Cai, Multicolor lanthanide-doped CaS and SrS near-
809 infrared stimulated luminescent nanoparticles with bright emission: application in broad-
810 spectrum lighting, information coding, and bio-imaging. *Nanoscale*. **11** (2019), pp. 12497–
811 12501.

812 39. X. Qiu, X. Zhu, M. Xu, W. Yuan, W. Feng, F. Li, Hybrid Nanoclusters for Near-Infrared to
813 Near-Infrared Upconverted Persistent Luminescence Bioimaging. *ACS Appl. Mater.*
814 *Interfaces*. **9**, 32583–32590 (2017).

40. W. Yang, R. Yuste, In vivo imaging of neural activity. *Nat. Methods*. **14**, 349–359 (2017).

41. J. K. Adams, V. Boominathan, S. Gao, A. V. Rodriguez, D. Yan, C. Kemere, A. Veeraraghavan, J. T. Robinson, In vivo fluorescence imaging with a flat, lensless microscope. *bioRxiv* (2020), p. 2020.06.04.135236.

42. G. Feng, R. H. Mellor, M. Bernstein, C. Keller-Peck, Q. T. Nguyen, M. Wallace, J. M. Nerbonne, J. W. Lichtman, J. R. Sanes, Imaging neuronal subsets in transgenic mice expressing multiple spectral variants of GFP. *Neuron*. **28**, 41–51 (2000).

43. K. W. Dunn, M. M. Kamocka, J. H. McDonald, A practical guide to evaluating colocalization in biological microscopy. *Am. J. Physiol. Cell Physiol.* **300**, C723–42 (2011).

44. X. Wu, X. Zhu, P. Chong, J. Liu, L. N. Andre, K. S. Ong, K. Brinson Jr, A. I. Mahdi, J. Li, L. E. Fenno, H. Wang, G. Hong, Sono-optogenetics facilitated by a circulation-delivered rechargeable light source for minimally invasive optogenetics. *Proc. Natl. Acad. Sci. U. S. A.* **116**, 26332–26342 (2019).

45. J. Szanics, T. Okubo, M. Kakihana, Preparation of LiTaO3 powders at reduced temperatures by a polymerized complex method. *J. Alloys Compd.* **281**, 206–210 (1998).

46. L. H. Wang, D. R. Yuan, X. L. Duan, X. Q. Wang, F. P. Yu, Synthesis and characterization of fine lithium niobate powders by sol- gel method. *Crystal Research and Technology*. **42** (2007), pp. 321–324.

47. A. Singer, S. Dutta, E. Lewis, Z. Chen, J. C. Chen, N. Verma, B. Avants, A. K. Feldman, J. O'Malley, M. Beierlein, C. Kemere, J. T. Robinson, Magnetoelectric Materials for Miniature, Wireless Neural Stimulation at Therapeutic Frequencies. *Neuron*. **107**, 631–643.e5 (2020).

48. X. Ou, X. Qin, B. Huang, J. Zan, Q. Wu, Z. Hong, L. Xie, H. Bian, Z. Yi, X. Chen, Y. Wu, X. Song, J. Li, Q. Chen, H. Yang, X. Liu, High-resolution X-ray luminescence extension imaging. *Nature*. **590**, 410–415 (2021).

49. N. Kohler, G. E. Fryxell, M. Zhang, A Bifunctional Poly(ethylene glycol) Silane Immobilized on Metallic Oxide-Based Nanoparticles for Conjugation with Cell Targeting Agents. *Journal of the American Chemical Society*. **126** (2004), pp. 7206–7211.

50. Y. Zhong, Z. Ma, F. Wang, X. Wang, Y. Yang, Y. Liu, X. Zhao, J. Li, H. Du, M. Zhang, Q. Cui, S. Zhu, Q. Sun, H. Wan, Y. Tian, Q. Liu, W. Wang, K. C. Garcia, H. Dai, In vivo molecular imaging for immunotherapy using ultra-bright near-infrared-IIb rare-earth nanoparticles. *Nat. Biotechnol.* **37**, 1322–1331 (2019).

51. J. Cohen, *Statistical Power Analysis for the Behavioral Sciences* (Academic Press, 2013).

52. T. Liu, L. Li, X. Teng, X. Huang, H. Liu, D. Chen, J. Ren, J. He, F. Tang, Single and repeated dose toxicity of mesoporous hollow silica nanoparticles in intravenously exposed mice. *Biomaterials*. **32**, 1657–1668 (2011).

53. F. J. Martin, K. Melnik, T. West, J. Shapiro, M. Cohen, A. A. Boiarski, M. Ferrari, Acute

Toxicity of Intravenously Administered Microfabricated Silicon Dioxide Drug Delivery Particles in Mice. *Drugs in R & D*. **6**, 71–81 (2005).

54. X. Wu, Y. Jiang, N. J. Rommelfanger, F. Yang, Q. Zhou, R. Yin, J. Liu, S. Cai, W. Ren, A. Shin, K. S. Ong, K. Pu, G. Hong, Tether-free photothermal deep-brain stimulation in freely behaving mice via wide-field illumination in the near-infrared-II window. *Nat Biomed Eng* (2022), doi:10.1038/s41551-022-00862-w.

55. O. Yizhar, L. E. Fenno, M. Prigge, F. Schneider, T. J. Davidson, D. J. O'Shea, V. S. Sohal, I. Goshen, J. Finkelstein, J. T. Paz, K. Stehfest, R. Fudim, C. Ramakrishnan, J. R. Huguenard, P. Hegemann, K. Deisseroth, Neocortical excitation/inhibition balance in information processing and social dysfunction. *Nature*. **477**, 171–178 (2011).

56. A. Berndt, O. Yizhar, L. A. Gunaydin, P. Hegemann, K. Deisseroth, Bi-stable neural state switches. *Nat. Neurosci.* **12**, 229–234 (2009).

57. X. Gong, D. Mendoza-Halliday, J. T. Ting, T. Kaiser, X. Sun, A. M. Bastos, R. D. Wimmer, B. Guo, Q. Chen, Y. Zhou, M. Pruner, C. W.-H. Wu, D. Park, K. Deisseroth, B. Barak, E. S. Boyden, E. K. Miller, M. M. Halassa, Z. Fu, G. Bi, R. Desimone, G. Feng, An Ultra-Sensitive Step-Function Opsin for Minimally Invasive Optogenetic Stimulation in Mice and Macaques. *Neuron*. **107**, 38–51.e8 (2020).

58. B. A. Hartl, H. Hirschberg, L. Marcu, S. R. Cherry, Characterizing low fluence thresholds for in vitro photodynamic therapy. *Biomed. Opt. Express*. **6**, 770–779 (2015).

59. E. H. Kim, S. Park, Y. K. Kim, M. Moon, J. Park, K. J. Lee, S. Lee, Y.-P. Kim, Self-luminescent photodynamic therapy using breast cancer targeted proteins. *Sci Adv*. **6** (2020), doi:10.1126/sciadv.aba3009.

60. J. Schubert, A. Lindenbaum, Stability of Alkaline Earth—Organic Acid Complexes Measured by Ion Exchange1. *J. Am. Chem. Soc.* **74**, 3529–3532 (1952).

61. J. L. Meyer, Formation constants for interaction of citrate with calcium and magnesium lons. *Anal. Biochem.* **62**, 295–300 (1974).

62. P. C. Bennett, M. E. Melcer, D. I. Siegel, J. P. Hassett, The dissolution of quartz in dilute aqueous solutions of organic acids at 25°C. *Geochim. Cosmochim. Acta*. **52**, 1521–1530 (1988).

63. A. Heller, A. Barkleit, H. Foerstendorf, S. Tsushima, K. Heim, G. Bernhard, Curium(iii) citrate speciation in biological systems: a europium(iii) assisted spectroscopic and quantum chemical study. *Dalton Transactions*. **41** (2012), p. 13969.

64. D. T. Sawyer, P. J. Paulsen, Properties and Infrared Spectra of Ethylenediaminetetraacetic Acid Complexes. II. Chelates of Divalent Ions1. *J. Am. Chem. Soc.* **81**, 816–820 (1959).

65. A. Gácsi, B. Kutus, Á. Buckó, Z. Csendes, G. Peintler, I. Pálinkó, P. Sipos, Some aspects of the aqueous solution chemistry of the Na /Ca2 /OH−/Cit3− system: The structure of a new calcium citrate complex forming under hyperalkaline conditions. *Journal of Molecular Structure*. **1118** (2016), pp. 110–116.

66. A. Bodor, I. Bányai, L. Zékány, I. Tóth, Slow dynamics of aluminium-citrate complexes studied by 1H- and 13C-NMR spectroscopy. *Coord. Chem. Rev.* **228**, 163–173 (2002).

67. F. R. Bacon, F. C. Raggon, Promotion of attack on glass and silica by citrate and other anions in neutral solution. *J. Am. Ceram. Soc.* **42**, 199–205 (1959).

68. L. Zamirri, A. Macià Escatllar, J. Mariñoso Guiu, P. Ugliengo, S. T. Bromley, What Can Infrared Spectra Tell Us about the Crystallinity of Nanosized Interstellar Silicate Dust Grains? *ACS Earth Space Chem.* **3**, 2323–2338 (2019).

69. A. I. Bortun, L. N. Bortun, A. Clearfield, Hydrothermal Synthesis of Sodium Zirconium Silicates and Characterization of Their Properties. *Chem. Mater.* **9**, 1854–1864 (1997).

70. Z. Li, N. Yu, J. Zhou, Y. Li, Y. Zhang, L. Huang, K. Huang, Y. Zhao, S. Kelmar, J. Yang, G. Han, Coloring Afterglow Nanoparticles for High-Contrast Time-Gating-Free Multiplex Luminescence Imaging. *Adv. Mater.* **32**, e2003881 (2020).

71. Y.-J. Li, C.-X. Yang, X.-P. Yan, Biomimetic Persistent Luminescent Nanoplatform for Autofluorescence-Free Metastasis Tracking and Chemophotodynamic Therapy. *Anal. Chem.* **90**, 4188–4195 (2018).

72. Y.-F. Gao, R. Zou, G.-F. Chen, B.-M. Liu, Y. Zhang, J. Jiao, K.-L. Wong, J. Wang, Large-Pore Mesoporous-Silica-Assisted synthesis of high-performance ZnGa2O4:Cr3+/Sn4+@MSNs multifunctional nanoplatform with optimized optical probe mass ratio and superior residual pore volume for improved bioimaging and drug delivery. *Chem. Eng. J.* **420**, 130021 (2021).

73. Y. Wang, C.-X. Yang, X.-P. Yan, Hydrothermal and biomineralization synthesis of a dual-modal nanoprobe for targeted near-infrared persistent luminescence and magnetic resonance imaging. *Nanoscale*. **9**, 9049–9055 (2017).

74. A. Abdukayum, J.-T. Chen, Q. Zhao, X.-P. Yan, Functional near infrared-emitting Cr3+/Pr3+ co-doped zinc gallogermanate persistent luminescent nanoparticles with superlong afterglow for in vivo targeted bioimaging. *J. Am. Chem. Soc.* **135**, 14125–14133 (2013).

75. Y. Feng, R. Liu, L. Zhang, Z. Li, Y. Su, Y. Lv, Raspberry-Like Mesoporous Zn1.07Ga2.34Si0.98O6.56:Cr0.01 Nanocarriers for Enhanced Near-Infrared Afterglow Imaging and Combined Cancer Chemotherapy. *ACS Appl. Mater. Interfaces*. **11**, 44978–44988 (2019).

76. Y.-J. Li, X.-P. Yan, Synthesis of functionalized triple-doped zinc gallogermanate nanoparticles with superlong near-infrared persistent luminescence for long-term orally administrated bioimaging. *Nanoscale*. **8,** 14965–14970 (2016).

77. J. Shi, X. Sun, S. Zheng, J. Li, X. Fu, H. Zhang, A new near-infrared persistent luminescence nanoparticle as a multifunctional nanoplatform for multimodal imaging and cancer therapy. *Biomaterials*. **152**, 15–23 (2018).

78. Y. Lv, D. Ding, Y. Zhuang, Y. Feng, J. Shi, H. Zhang, T.-L. Zhou, H. Chen, R.-J. Xie,

928 Chromium-Doped Zinc Gallogermanate@Zeolitic Imidazolate Framework-8: A
929 Multifunctional Nanoplatform for Rechargeable In Vivo Persistent Luminescence Imaging
930 and pH-Responsive Drug Release. *ACS Appl. Mater. Interfaces*. **11**, 1907–1916 (2019).

931 79. M. Pellerin, E. Glais, T. Lecuyer, J. Xu, J. Seguin, S. Tanabe, C. Chanéac, B. Viana, C.
932 Richard, LaAlO3:Cr3+, Sm3+: Nano-perovskite with persistent luminescence for in vivo
933 optical imaging. *J. Lumin.* **202**, 83–88 (2018).

934 80. T. Ai, W. Shang, H. Yan, C. Zeng, K. Wang, Y. Gao, T. Guan, C. Fang, J. Tian, Near
935 infrared-emitting persistent luminescent nanoparticles for Hepatocellular Carcinoma imaging
936 and luminescence-guided surgery. *Biomaterials*. **167**, 216–225 (2018).

937 81. T. Maldiney, A. Lecointre, B. Viana, A. Bessière, M. Bessodes, D. Gourier, C. Richard, D.
938 Scherman, Controlling electron trap depth to enhance optical properties of persistent
939 luminescence nanoparticles for in vivo imaging. *J. Am. Chem. Soc.* **133**, 11810–11815
940 (2011).

941 82. Z. Xue, X. Li, Y. Li, M. Jiang, H. Liu, S. Zeng, J. Hao, X-ray-Activated Near-Infrared
942 Persistent Luminescent Probe for Deep-Tissue and Renewable in Vivo Bioimaging. *ACS*
943 *Appl. Mater. Interfaces*. **9**, 22132–22142 (2017).

944 83. B. Zheng, Y. Bai, H. Chen, H. Pan, W. Ji, X. Gong, X. Wu, H. Wang, J. Chang, Near-
945 Infrared Light-Excited Upconverting Persistent Nanophosphors in Vivo for Imaging-Guided
946 Cell Therapy. *ACS Appl. Mater. Interfaces*. **10**, 19514–19522 (2018).

947 84. X. Chen, Y. Li, K. Huang, L. Huang, X. Tian, H. Dong, R. Kang, Y. Hu, J. Nie, J. Qiu, G.
948 Han, Trap Energy Upconversion-Like Near-Infrared to Near-Infrared Light Rejuvenateable
949 Persistent Luminescence. *Adv. Mater.* **33**, e2008722 (2021).

950 85. C. Xie, X. Zhen, Q. Miao, Y. Lyu, K. Pu, Self-Assembled Semiconducting Polymer
951 Nanoparticles for Ultrasensitive Near-Infrared Afterglow Imaging of Metastatic Tumors.
952 *Adv. Mater.* **30**, e1801331 (2018).

953 86. X. Zhen, Y. Tao, Z. An, P. Chen, C. Xu, R. Chen, W. Huang, K. Pu, Ultralong
954 Phosphorescence of Water-Soluble Organic Nanoparticles for In Vivo Afterglow Imaging.
955 *Adv. Mater.* **29,** 201606665 (2017).

956 87. F. Zhang, M. Xu, X. Su, W. Yuan, W. Feng, Q. Su, F. Li, Afterglow Implant for Arterial
957 Embolization and Intraoperative Imaging. *Chemistry*. **28**, e202103795 (2022).

958 88. X. Wang, W. Yuan, M. Xu, X. Su, F. Li, Visualization of Acute Inflammation through a
959 Macrophage-Camouflaged Afterglow Nanocomplex. *ACS Appl. Mater. Interfaces*. **14**, 259–
960 267 (2022).

961 89. X. Ni, X. Zhang, X. Duan, H.-L. Zheng, X.-S. Xue, D. Ding, Near-Infrared Afterglow
962 Luminescent Aggregation-Induced Emission Dots with Ultrahigh Tumor-to-Liver Signal
963 Ratio for Promoted Image-Guided Cancer Surgery. *Nano Lett.* **19**, 318–330 (2019).

964

**Acknowledgments**

We thank the Stanford Animal Histology Services for help with preparation of histologic specimens. Part of this work was performed at the Stanford Nano Shared Facilities (SNSF), supported by the National Science Foundation under award ECCS-2026822. Confocal imaging was performed at the Stanford Wu Tsai Neuroscience Microscopy Service. **Funding:** G.H. acknowledges two awards by NIH (5R00AG056636-04 and 1R34NS127103-01), a National Science Foundation (NSF) CAREER award (2045120), an NSF EAGER award (2217582), a Rita Allen Foundation Scholars Award, a Beckman Technology Development Grant, a grant from the focused ultrasound (FUS) Foundation, a gift from the Spinal Muscular Atrophy (SMA) Foundation, a gift from the Pinetops Foundation, two seed grants from the Wu Tsai Neurosciences Institute, and a seed grant from the Bio-X Initiative of Stanford University. X.W. acknowledges the support by a Stanford Graduate Fellowship. Z.O. acknowledges the support by a Wu Tsai Neurosciences Institute Interdisciplinary Scholar Award. Some schematics were created with BioRender.com. **Author contributions:** F.Y., X.W., and G.H. conceived and designed the project, F.Y., X.W., H.C., Z.O., S.C., Q.Z., and B.G.W. performed the experiments. F.Y., X.W., H.C., Z.O., S.C., Q.Z., H.H., and G.H. analyzed the data. F.Y., X.W., H.C., and G.H. wrote the manuscript. All authors discussed the results and commented on the manuscript. **Competing interests:** The authors declare no competing interests. **Data and materials availability:** All data needed to evaluate the conclusions in the paper are present in the paper and the Supplementary Materials.

984 **Figures and Tables**

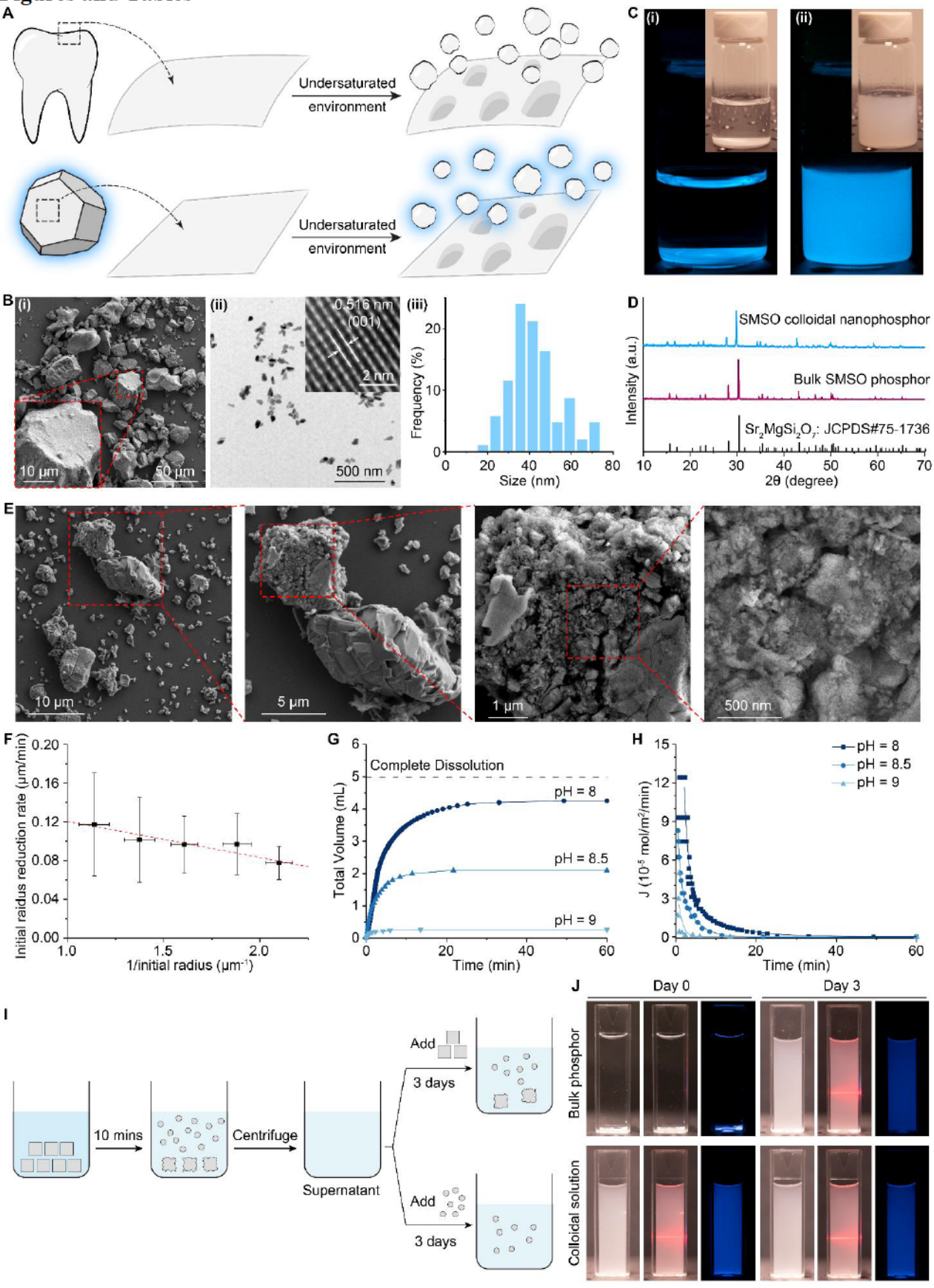

**Fig. 1**. **BID approach for synthesizing colloidal SMSO solutions**. (**A**) Schematics showing the BID mechanism for dissolving tooth enamel (top) and sparingly soluble phosphors (bottom) into nanoparticles in an undersaturated solution. (**B**) SEM (i) and TEM (ii) images of the bulk SMSO phosphor and its colloidal nanoparticles, respectively. The inset in ii shows the HRTEM image of a SMSO nanoparticle. A histogram showing the size distribution of SMSO colloids is shown in iii. (**C**) Afterglow images and brightfield images (insets) of an aqueous suspension of bulk SMSO phosphor (i) and its stable colloidal solution of nanophosphors (ii). (**D**) XRD spectra of bulk SMSO phosphor and its colloidal nanoparticles. An average domain size of 52 nm was obtained by analyzing peak widths in the XRD spectrum of SMSO colloids with the Scherrer equation. (**E**) SEM images of bulk SMSO particles after reaching a metastable equilibrium. (**F**) Plot showing the average instantaneous dissolution rate of SMSO particles as a function of their average inverse radius. The data is represented as mean values +/- standard deviation (SD). (**G**) Plots of the titrant volume as a function of time for kinetically preserved dissolution of SMSO at different pH. (**H**) Plots of the flux rate (J) as a function of time for SMSO dissolution at different undersaturations. (**I**) Schematic showing the steps of an experimental procedure that verifies the BID mechanism. (**J**) Brightfield image (left), Tyndall effect (middle), and afterglow image (right) of colloidal solutions prepared under different conditions (see Materials and Methods).

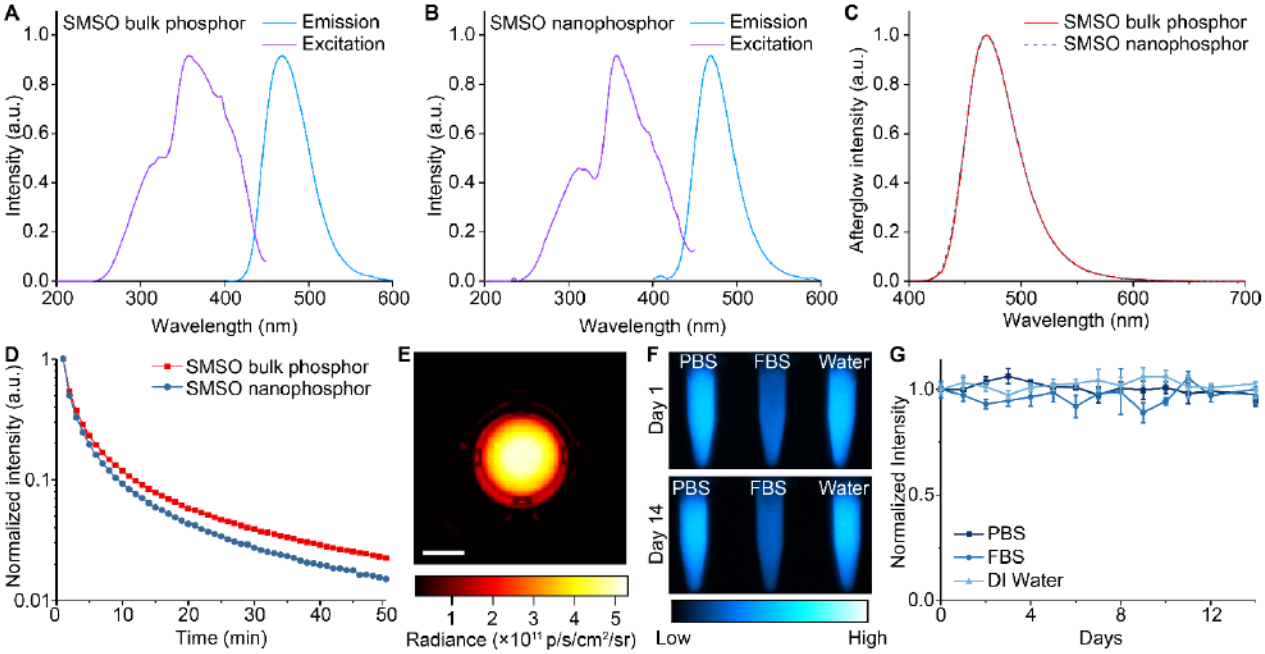


**Fig. 2. Strong and persistent afterglow of BID-produced SMSO nanophosphor colloids**. (**A**) The excitation and emission spectra of untreated, bulk SMSO phosphor. (**B**) The excitation and emission spectra of a colloidal solution of SMSO nanophosphors. (**C**) The afterglow spectra of SMSO bulk phosphor and colloidal nanophosphor. (**D**) Afterglow curves of SMSO bulk phosphor and colloidal nanophosphor. (**E**) Afterglow image of a colloidal solution of SMSO nanophosphors (493 nmol/L) in a 48 well plate acquired by the IVIS imaging system. The scale bar represents 0.5 cm. (**F**) Afterglow images of colloidal solutions of SMSO nanophosphors in PBS (left), FBS (middle) and water (right) at Day 1 (top) and Day 14 (bottom). The decrease in afterglow intensity for FBS is due to the absorption of FBS at the emission wavelengths of SMSO colloids and does not reflect the instability of SMSO afterglow (fig. S10). (**G**) Chronic stability of normalized afterglow intensity of SMSO colloidal solutions in PBS, FBS and water. All data are presented as mean values +/- SD.

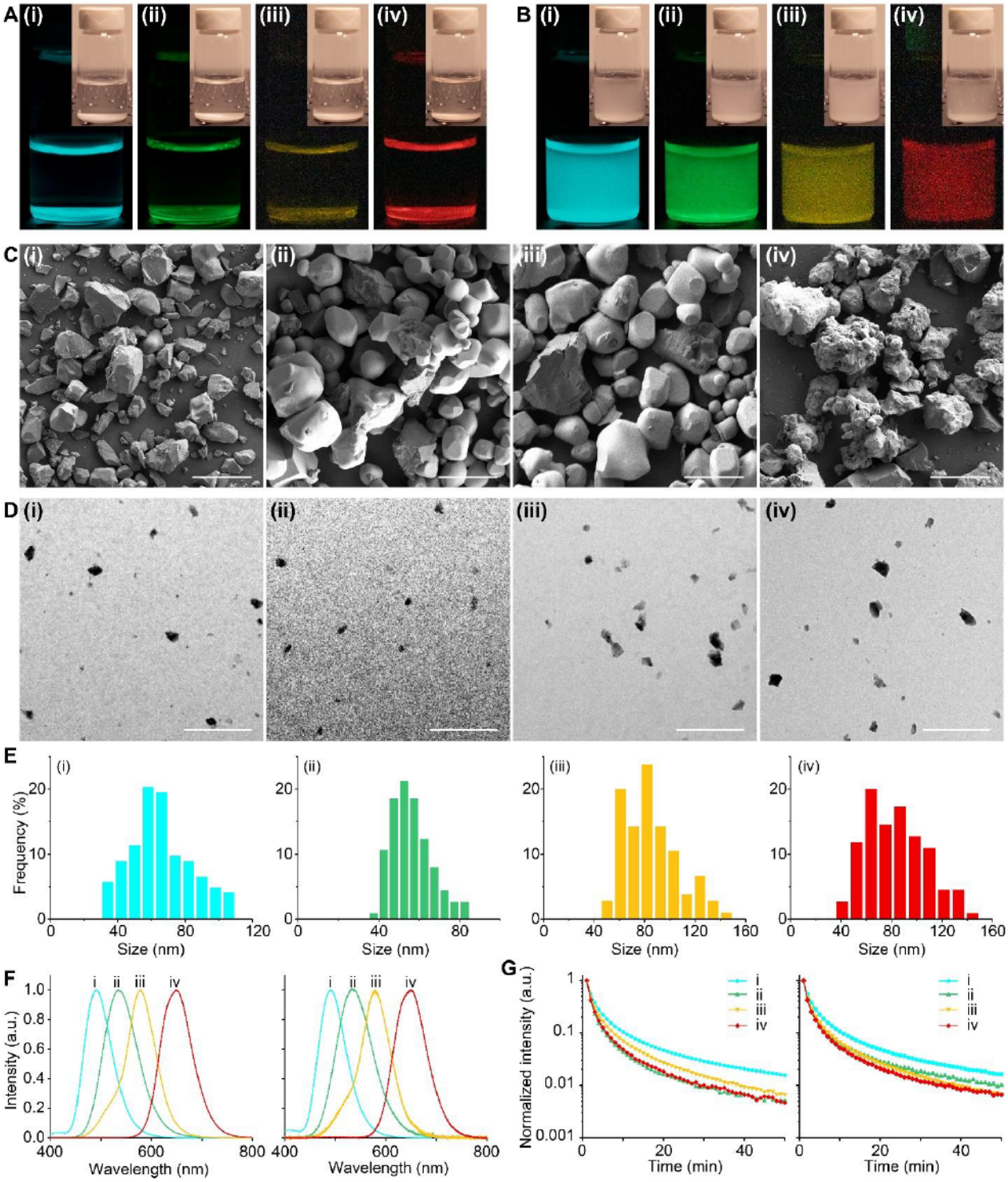


**Fig. 3. Generalizability of the BID method**. (**A**) Afterglow images and their corresponding brightfield images (insets) of SAO (i), ZnS:Cu,Al (ii), ZnS:Mn (iii), and CSS (iv) bulk phosphors. (**B**) Afterglow images and their corresponding brightfield images (insets) of SAO (i), ZnS:Cu,Al (ii), ZnS:Mn (iii), and CSS (iv) nanophosphor colloids. (**C**) SEM images of SAO (i), ZnS:Cu,Al (ii), ZnS:Mn (iii), and CSS (iv) bulk phosphors. The scale bars represent 50 µm. (**D**) TEM images of SAO (i), ZnS:Cu,Al (ii), ZnS:Mn (iii), and CSS (iv) nanophosphor colloids. The scale bars represent 500 nm. (**E**) Histograms showing the size distributions of SAO (i), ZnS:Cu,Al (ii),

ZnS:Mn (iii), and CSS (iv) nanophosphor colloids. Each histogram is based on 100 colloidal nanoparticles in the TEM images. (**F**) Afterglow spectra of SAO (i), ZnS:Cu,Al (ii), ZnS:Mn (iii), and CSS (iv) bulk phosphors (left) and colloidal nanophosphors (right). (**G**) Luminescence decay curves of SAO (i), ZnS:Cu,Al (ii), ZnS:Mn (iii), and CSS (iv) bulk phosphors (left) and colloidal nanophosphors (right).

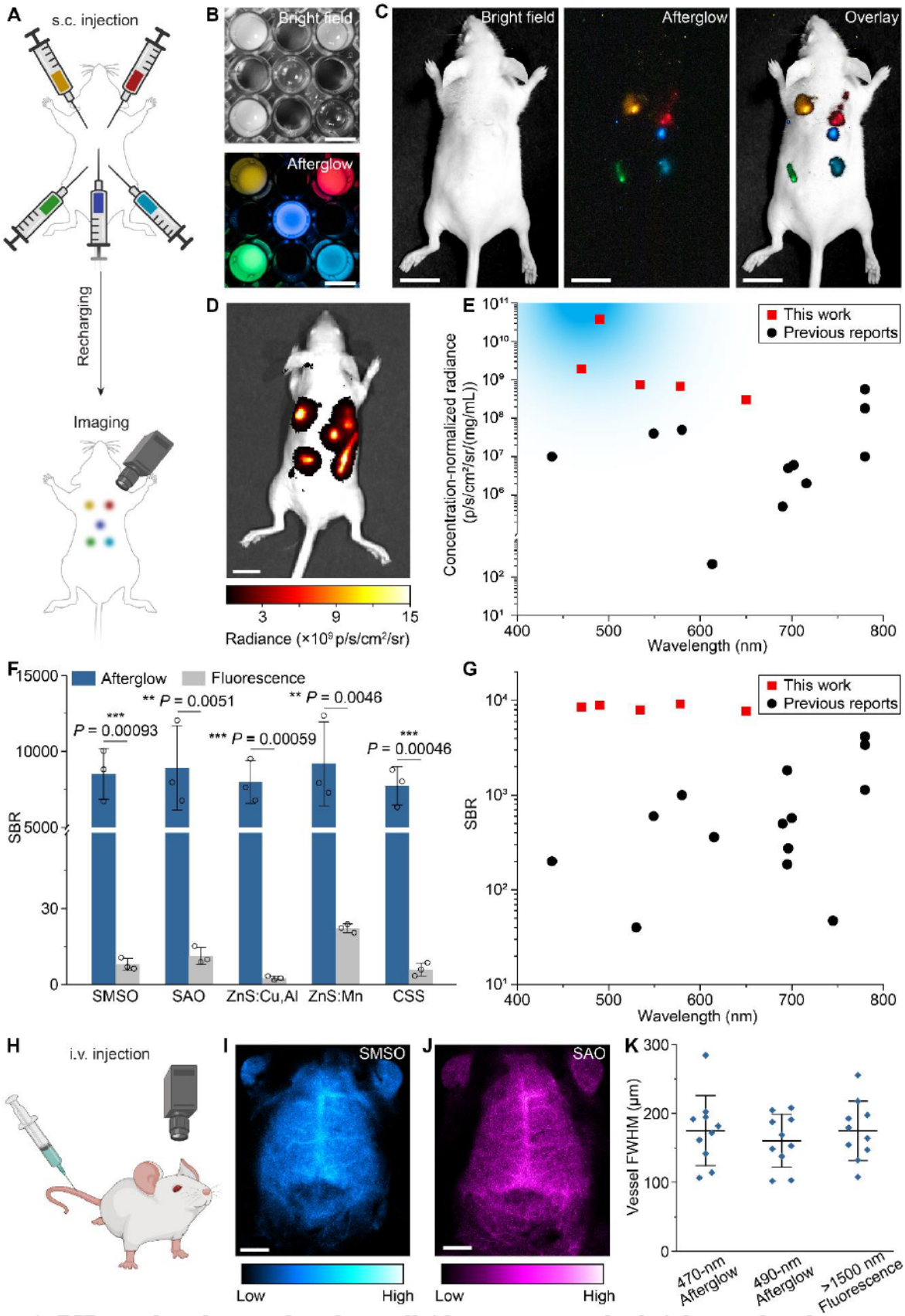


**Fig. 4. BID-produced nanophosphor colloids are among the brightest afterglow materials after delivery *in vivo*.** (**A**) BID-produced colloids can be delivered via subcutaneous

administration. (**B**) Brightfield (top) and afterglow (bottom) images of five colloidal solutions in a multiwell plate. (**C**) Brightfield (left), afterglow (middle), and overlay (right) images of subcutaneously administered colloidal solutions. (**D**) Afterglow image of subcutaneously injected colloids acquired using the IVIS imaging system. (**E**) Scatter plot of concentration-normalized afterglow radiance vs. emission wavelength for subcutaneously injected colloids in this work and previous reports. The blue shade represents the desirable power density for activating SSFO and psCas9 in various biological applications. (**F**) Statistical analysis of the SBR for afterglow and fluorescence imaging with BID-produced nanophosphor colloids. All data are presented as mean values +/- SD. $n = 3$ for all groups. $^{**}P < 0.01$; $^{***}P < 0.001$. (**G**) Scatter plot of the SBR vs. emission wavelength for subcutaneously injected colloidal solutions of nanophosphors in this work and previous reports. (**H**) BID-produced colloidal solutions of nanophosphors can be delivered via intravenous administration for brain imaging. (**I&J**) Transcranial afterglow images of brain vascular structures after intravenous injection of SMSO (**I**) and SAO (**J**) colloidal solutions. (**K**) The full-width at half maximum (FWHM) of the smallest discernible cerebral vessels in afterglow images of this work and an NIR-II (>1500 nm) fluorescence image in Ref. (*50*) under the same level of magnification. The scale bars are 1 cm in (**B&D**), 1.5 cm in (**C**) and 2.5 mm in (**I&J**).

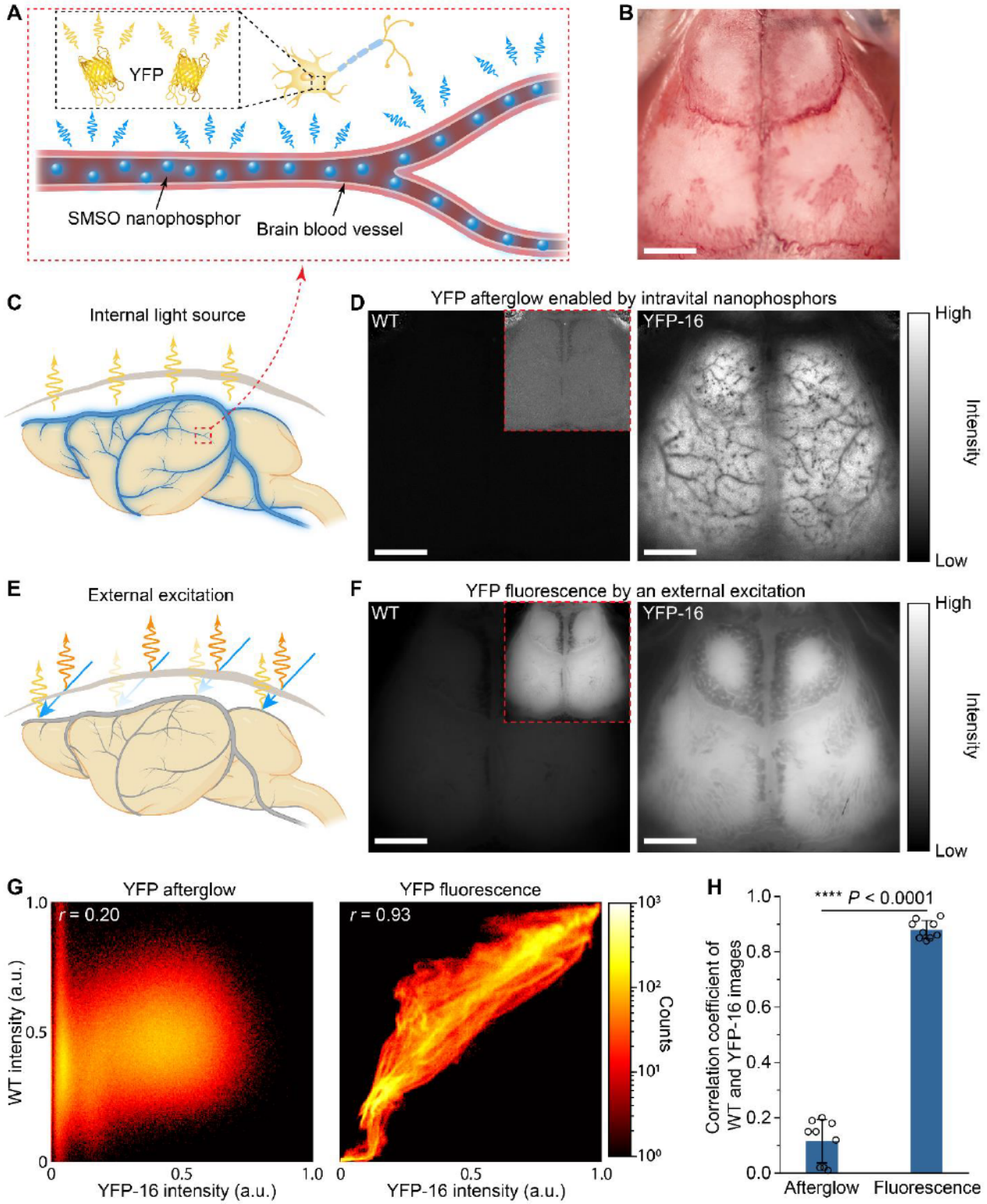


**Fig. 5. BID-produced colloids as an intravital light source for YFP imaging**. (**A**) Schematic showing SMSO colloids in blood vessels as an internal light source for exciting YFP fluorescence *in situ*. (**B**) Photo of the mouse head with the intact skull, which is dominated by the intrinsic skull features. (**C&E**) Schematic of brain fluorescence imaging with an internal light source (**C**) or a conventional external light source (**E**). The blue glow represents the internal excitation light. The blue, yellow, and orange arrows represent external excitation light, YFP fluorescence, and skull

autofluorescence, respectively. The fluorescence image excited by a conventional external light source (**E**) is contaminated by skull features due to spatially varying skull attenuation and autofluorescence. (**D&F**) YFP afterglow (**D**) or fluorescence (**F**) images of the WT (left) and YFP-16 (right) mouse brains excited by the intravenously delivered colloidal light source (**D**) or an external light source (**F**). The insets in the left panels are WT images with digitally enhanced brightness to match YFP-16 images. All images in **B,D&F** were taken with the intact skull. All scale bars represent 2 mm. (**G**) Intensity scatter plot of the WT and YFP-16 images under the afterglow (left) or fluorescence (right) modes. The Pearson's correlation coefficient *r* is provided on the image. (**H**) Statistical analysis of Pearson's correlation coefficients (indicating similarity) between the WT and YFP-16 images under the afterglow or fluorescence modes. All data are presented as mean values +/- SD. ****, $P < 0.0001$.

Science Advances
AAAS

# Supplementary Materials for

## A biomineral-inspired approach of synthesizing colloidal persistent phosphors as a multicolor, intravital light source

Fan Yang[1,2]†, Xiang Wu[1,2]†, Han Cui[1,2], Zihao Ou[1,2], Shan Jiang[1,2], Sa Cai[1,2], Qi Zhou[1,2], Bryce G. Wong[1,2], Hans Huang[1,2], and Guosong Hong[1,2]*

*Corresponding author. Email: guosongh@stanford.edu

**This PDF file includes:**

**Supplementary Text**

**Estimation of the ratio of bulk SMSO precursor particles to kinetically preserved SMSO nanoparticles**

In compliance with the kinetic preservation model of the BID method, two plausible but not mutually exclusive models exist to explain the origin of produced nanoparticles. Specifically, each micron-sized particle may be etched to a single nanoparticle with its size resistant to further dissolution. Alternatively, during dissolution of a micron particle, it may "shed" multiple nanoparticles from its surface as the pit expands. To this end, we calculated the final concentration of nanoparticles after the BID process as follows:

In a typical BID experiment described in Materials and Methods, an overall yield of 13% was found for SMSO nanophosphors, and the initial particle concentration of bulk SMSO precursor particles and kinetically preserved SMSO nanoparticles were $5.59 \times 10^6$ and $9.08 \times 10^{12}$ particles/mL, respectively, based on UV-Vis absorption measurement and their respective sizes. This result indicates that on average, every single micron-sized SMSO particle produces ~ $10^6$ nanoparticles during the kinetically preserved dissolution process. Therefore, although the first model cannot be excluded, the second model dominates the BID process to produce many small nanoparticles from their parent micron-sized particles. Further evidence is found from a close-up view of the large particles during dissolution, revealing many small nanoparticles loosely attached to the surfaces (Fig. 1E, the far right panel). A similar phenomenon has been observed during demineralization of tooth enamel, in which nanosized particles were released into the solution by fluid diffusion flux (*25*).

**Estimation of highest achievable afterglow power density *in vivo* after intravenous delivery for biological applications**

We first estimate the afterglow emission power per unit mass of nanophosphors ($\frac{P}{m_{BID}}$) using the *ex vivo* radiance measurement data (i.e., Fig. 2E) as follows:

$$\int_0^{h_0}\int_0^{r_0} 10^{-\varepsilon_{BID}\cdot\sqrt{r^2+h^2}\cdot C_{BID}} \frac{P}{m_{BID}} C_{BID} \frac{2\pi r}{4\pi(r^2+h^2)} dr\, dh = \Omega \cdot hc/\lambda \cdot L_\Omega$$

where $h_0$ and $r_0$ are the height and radius of the BID-produced nanophosphor solution in a 48 well plate, respectively; $\varepsilon_{BID}$ is the absorption coefficient of the BID-produced nanophosphor solution at its corresponding peak emission wavelength; $C_{BID}$ is the concentration of the nanophosphor solution; $\Omega = 4\pi$ is the solid angle; $hc/\lambda$ is the energy of a single photon at the peak emission wavelength, and $L_\Omega$ is the radiance measured by the IVIS system.

Then the highest achievable afterglow power density in different organs *in vivo* after intravenous delivery is estimated as follows:

$$I = \int_0^{l_0} \frac{P}{m_{BID}} C_{BID,blood}\, v/v_{blood}\, exp(-\mu_{eff}\, l)\, dl$$

where $l_0$ is the estimated dimension of the mouse organ; $C_{BID,blood}$ is the estimated highest achievable concentration of BID-produced nanophosphor solution in the blood based on previous reports (*52*, *53*); $v/v_{blood}$ is the volume percentage of blood in specific organs; $\mu_{eff}$ is the effective attenuation coefficient of specific organ tissue at the peak emission wavelength of the nanophosphor based on previous reports (*54*). The results for the blue-emitting nanophosphors are summarized below in table S1:

**Table S1. Estimated power densities of systemically delivered nanophosphors in different organs.**

| | Brain ($\mu W/cm^2$) | Liver ($\mu W/cm^2$) |
|---|---|---|
| SMSO | 0.627 | 1.01 |
| SAO | 21.8 | 36.2 |

Furthermore, we have also compared the estimated highest achievable power density above with the power needed for various biological applications.

First, for optogenetics neuromodulation, it has been previously reported that channelrhodopsins with slow dynamics (such as SSFO, stable step-function opsin) can act as photon integrators, and their photocurrent is determined by the total photon exposure even under extremely low light conditions (*55*, *56*). Specifically, it has been experimentally verified that the apparent time constants for activation of SSFO under ~1.6 and 2.9 $\mu W/cm^2$ 470-nm light are ~59 and 38 s, respectively (*55*). As calculated above, BID-produced SAO nanophosphor colloid can provide enough photons to activate SSFO across the entire brain within 5 s upon intravenous delivery. Furthermore, the recently developed ultra-sensitive step-function opsin (SOUL) requires even less photon exposure at 470-nm than SSFO (*57*), thus enabling SOUL to be activated with a lower SAO dosage or a shorter time interval after delivery.

Second, for light-mediated gene-editing, the single-chain psCas9 based on pdDronpa can be activated with 10 $\mu W/cm^2$ 500-nm light (*13*). The calculations above suggest that the intravenous delivery of SAO can provide enough power density in both the brain and the liver for activating psCas9.

Third, for photodynamic therapy, previous *in vitro* studies have demonstrated that the low fluence threshold for a commercially available photosensitizer $TPPS_{2a}$ under ~0.28 $\mu W/cm^2$ blue light illumination was 12 $mJ/cm^2$ (*58*). Such power density and light fluence should be achievable within ~5.5 min after intravenous delivery of SAO nanophosphors, while the *in vivo* afterglow intensity can be maintained at a relatively high level by applying constant remote recharging and leveraging the intrinsic circulatory system, as demonstrated in fig. S16. Furthermore, another recent report utilized bioluminescence to locally activate photosensitizer for photodynamic therapy *in vivo*, and the effective bioluminescence radiation was estimated to be as low as 15.6 $mJ/cm^2$ (26 $\mu W/cm^2$ for 10 min) at 500 nm (*59*). This light fluence requirement can also be achieved by using SAO nanophosphors as an internal light source after intravenous injection with constant remote recharging.

In summary, our calculations above suggest the feasibility of applying the blue-emitting nanophosphor colloids reported in this work as circulation-delivered internal light sources for various advanced biological applications, such as optogenetics neuromodulation based on SSFO or SOUL, light-mediated genome modification based on psCas9, and photodynamic therapy. Compared with conventional methods of light delivery, the systemically delivered internal light source is advantageous as it can reach deep tissue through blood circulation, illuminate the whole organ of interest uniformly, and does not require invasive implants such an LED or an optical fiber. Nonetheless, the advanced biological applications proposed above remain to be explored in future studies.

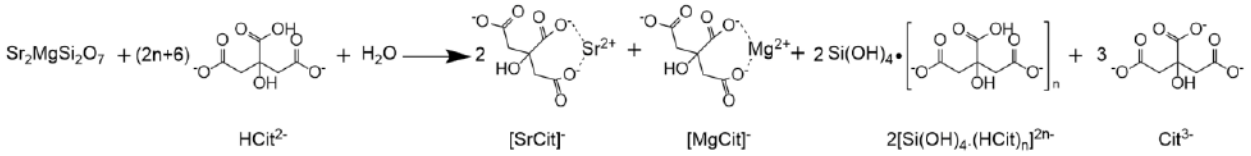


**Fig. S1. Hypothesized reaction during the BID process.** $HCit^{2-}$ represents the doubly-deprotonated citrate anion, and $Cit^{3-}$ represents the triply-deprotonated citrate anion. $Sr^{2+}$ and $Mg^{2+}$ cations form coordination complexes with the citrate anion with 1:1 stoichiometry (*60*). Triply-deprotonated citrate anions are the dominant form in these complexes in our pH range of interest (e.g., 6~10) (*61*). In addition, it has been reported that silica forms complexes with citrate with unknown stoichiometry (thus the subscript of *n*) to dissolve in an aqueous solution (*62*).

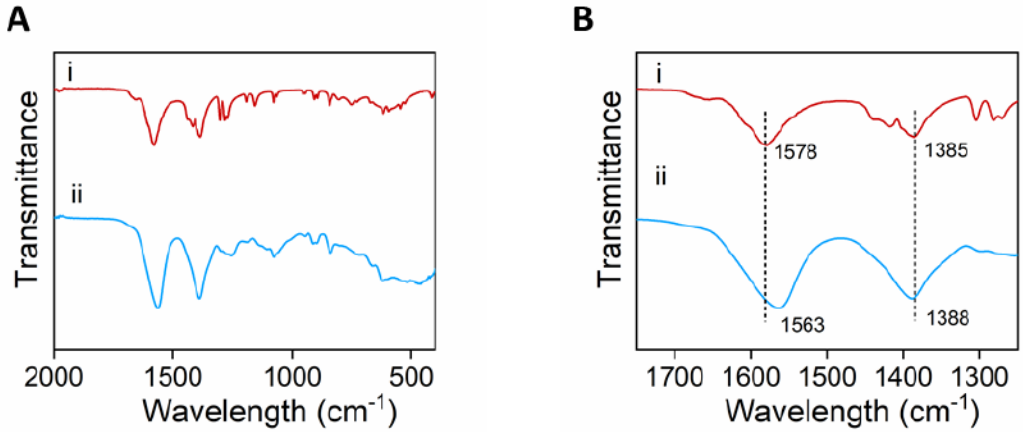


**Fig. S2. FTIR spectra of trisodium citrate and the BID solution.** Full-range (**A**) and close-up view (**B**) of FTIR spectra of trisodium citrate (i) and the citrate etchant after dissolving SMSO bulk particles (ii), revealing the chemical identity of coordinated metal cations in the solution after dissolution. The significant downshift of the antisymmetric stretching band of $-COO^-$ [i.e., $\upsilon_{as}(-COO^-)$] from 1578 $cm^{-1}$ to 1563 $cm^{-1}$ indicates the formation of the metal-carboxylate bond (*63*, *64*). Therefore, coordinated metal cations such as −COOMg, −COOSr, −COOEu, and −COODy should exist in the solution after dissolution. In addition, the upshift of the symmetric stretching band of $-COO^-$ [i.e., $\upsilon_s(-COO^-)$] from 1385 $cm^{-1}$ to 1388 $cm^{-1}$ is attributed to the formation of the metal-carboxylate bond. Based on this data, we postulate that metal-citrate complex ions are the most probable form of dissolved metals after dissolution of bulk SMSO.

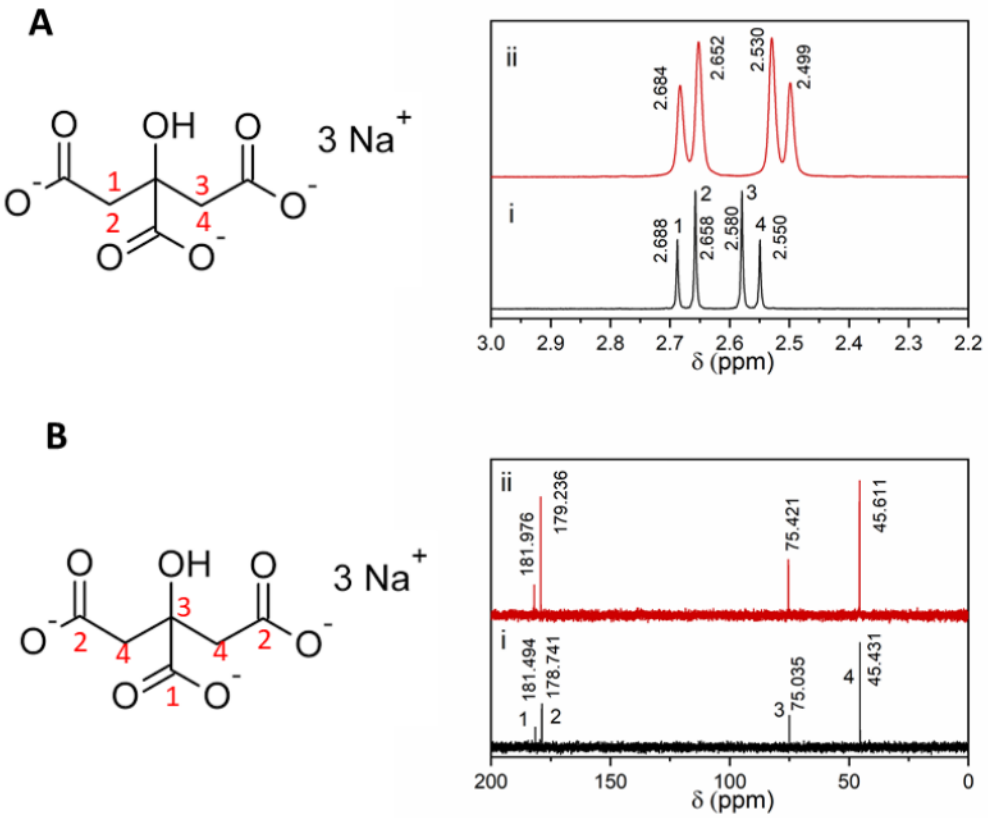


**Fig. S3. NMR spectra of trisodium citrate and the BID solution.** $^{1}$H (**A**) and $^{13}$C (**B**) NMR spectra of trisodium citrate (i) and the citrate etchant after dissolving SMSO bulk particles (ii), confirming the formation of metal-carboxyl bonds in the solution. Previous work reported a downshift of α-H atoms with peak broadening and an upshift of all C atoms when citrate forms coordination complexes with metal cations (*65*, *66*).

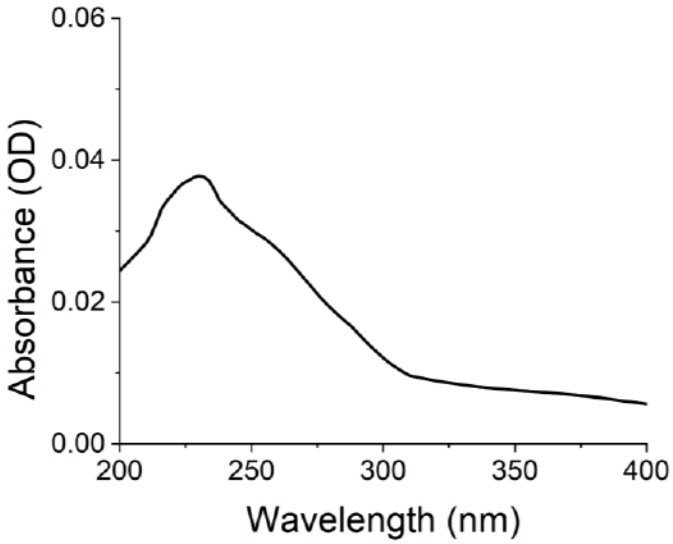


**Fig. S4. UV absorption spectrum of the BID solution.** UV absorption spectrum of the citrate etchant after dissolving SMSO bulk phosphor reveals the formation of silicate-citrate complexes. Such complexes were implied by a previous work studying the dissolution of silica by citrate (*67*), while an absorption peak near 240 nm suggests the formation of silicate-citrate complexes due to charge transfer (*62*).

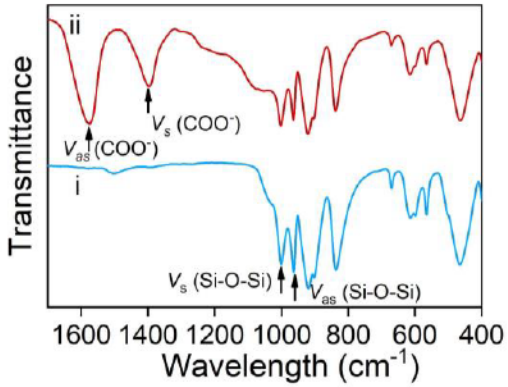


**Fig. S5. FTIR spectra of SMSO bulk phosphor (i) and colloidal nanophosphor (ii).** Peaks at 964 cm$^{-1}$ and 1000 cm$^{-1}$ correspond to Si-O-Si stretching modes (*68*, *69*), which are missing from the IR spectrum of the etched solution (fig. S2). This result suggests the absence of Si-O-Si bonds in the soluble products after dissolution, thus confirming a soluble form of silica-citrate complex in fig. S1. Additionally, the presence of symmetric and antisymmetric stretching bands of $-COO^-$ [i.e., $\upsilon_s(-COO^-)$ and $\upsilon_{as}(-COO^-)$] as labeled in ii suggests the adsorption of citrate anions on the surface of SMSO colloid to improve its colloidal stability when dispersed in water.

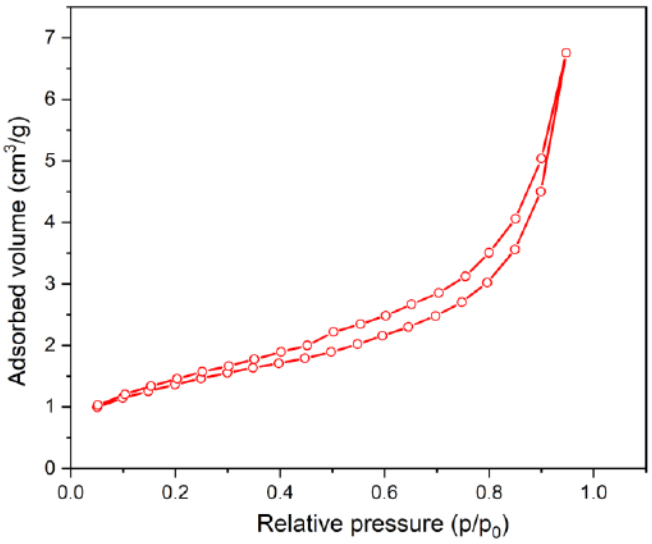


**Fig. S6. BET isotherm of SMSO bulk particles prior to the BID process.** We obtained a specific surface area of 43,850 $cm^2/g$ from this isotherm, thus yielding a total surface area of 4,385 $cm^2$ for kinetically preserved dissolution in the CC experiments.

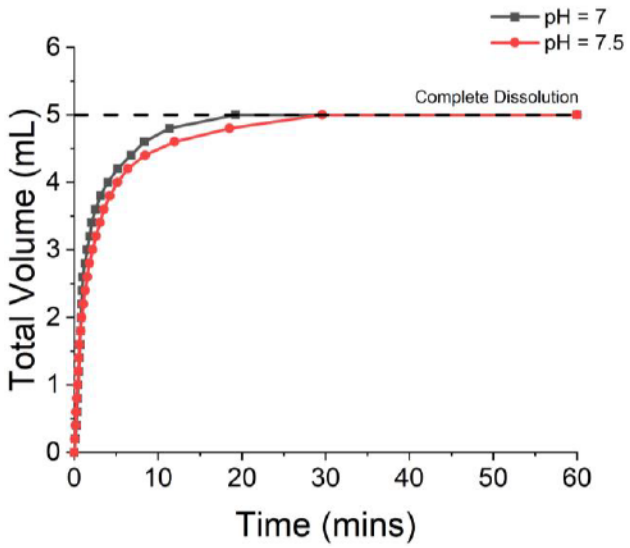


**Fig. S7. Titration curves at lower pH.** Plots of titrant volume as a function of time for complete dissolution of SMSO at pH 7 and pH 7.5 with the CC technique (see Materials and Methods).

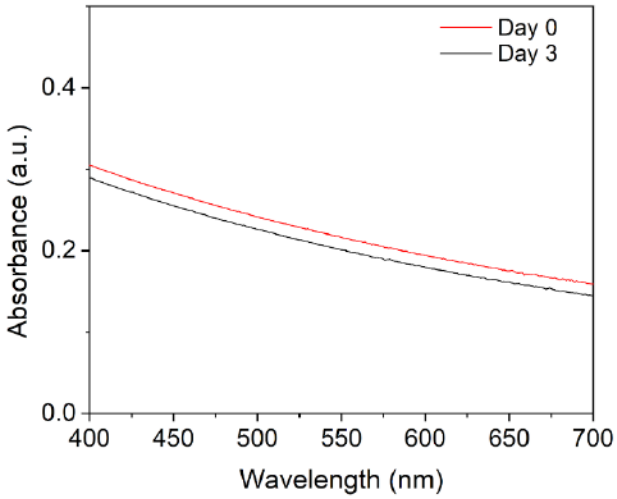


**Fig. S8. UV absorption spectra of SMSO colloidal solutions.** UV spectra of two solutions corresponding to Fig. 1J, bottom row, reveal the resistance of critically sized nanoparticles to further dissolution. Note that the 400-nm absorbance of SMSO colloidal solution in water is proportional to its molar concentration by an extinction coefficient of $2.7 \times 10^8$ L/mol/cm.

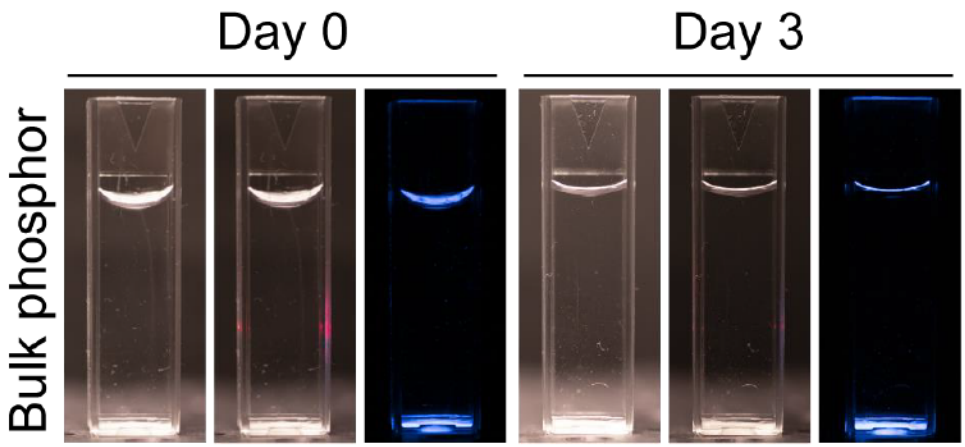


**Fig. S9. Images of bulk SMSO particles in pure water.** Bright-field image (left), Tyndall effect (middle), and afterglow image (right) of bulk SMSO particles in pure water without citrate (pH = 7) before and after mixing for 3 days under the same experimental conditions as the BID process with citrate, showing negligible dissolution of SMSO in pure water. This result ruled out the possibility of SMSO dissolving in pure water, which is consistent with the limited aqueous solubility of alkaline earth silicates. The lack of dissolution in pure water strongly contrasts with complete dissolution in citrate buffer at the same pH (fig. S7). Taken together, these results confirm the hypothesis that citrate ions provide the main drive for a negative $\triangle g$, while the pH modulates undersaturation due to the consumption of protons in the reaction (fig. S1).

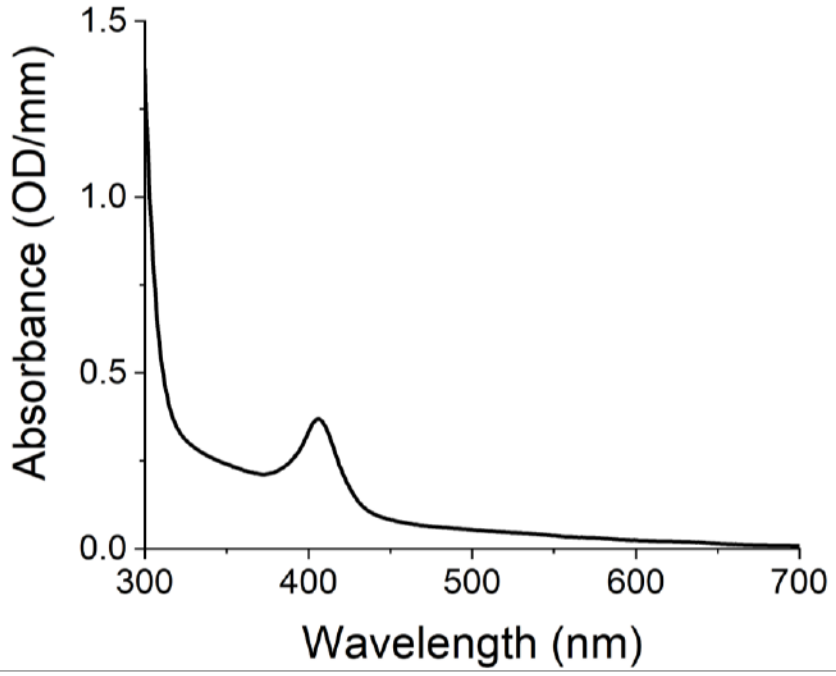


**Fig. S10. The absorption spectrum of FBS in the 300-700 nm range with a 1 mm optical path.** Note the absorbance of 0.06 $mm^{-1}$ at 470 nm, the emission wavelength of the SMSO colloid. This absorbance value corresponds to the attenuation of 56% in a microcentrifuge tube, agreeing with ~50% reduction in the afterglow of SMSO colloid in FBS observed in Fig. 2F.

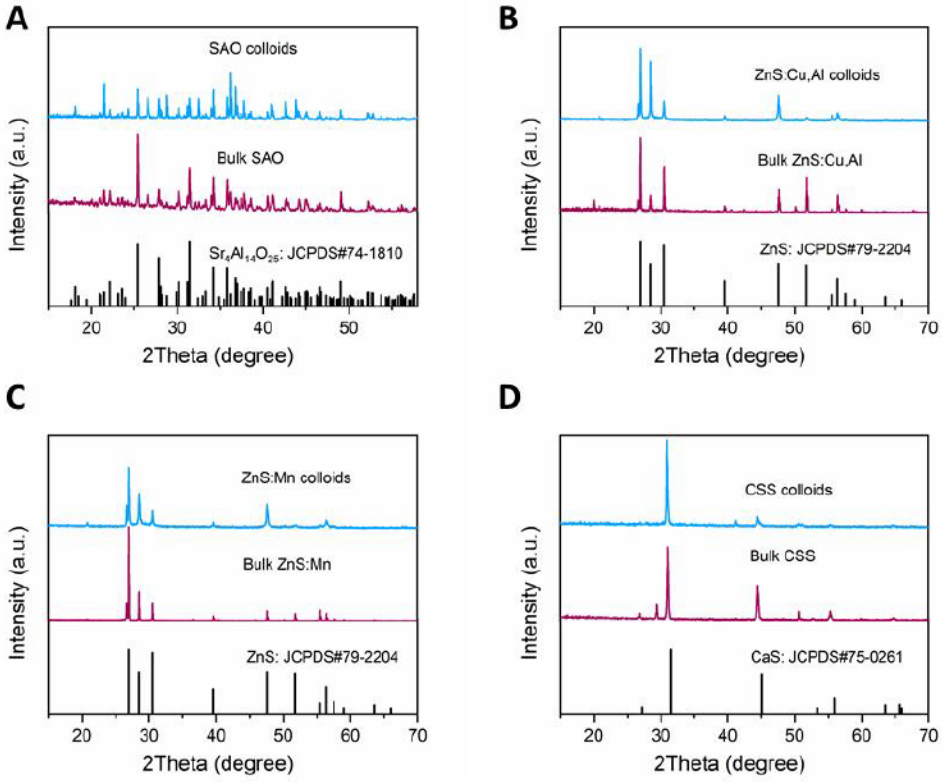


**Fig. S11. XRD spectra of different phosphors.** XRD spectra of bulk phosphors and their corresponding colloids for different materials: (**A**) SAO; (**B**) ZnS:Cu,Al; (**C**) ZnS:Mn; and (**D**) CSS.

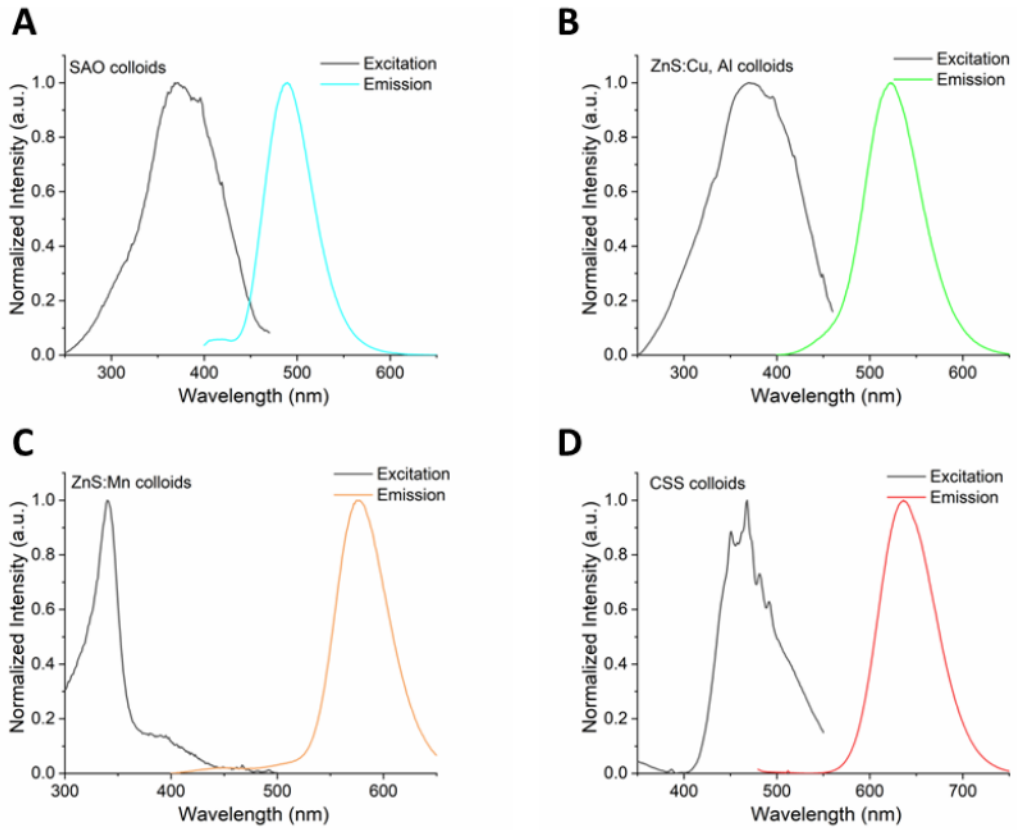


**Fig. S12. Photoluminescence characterization of different colloidal nanophosphors.** The excitation and emission spectra of different nanophosphor colloids produced by the BID approach: (**A**) SAO; (**B**) ZnS:Cu,Al; (**C**) ZnS:Mn; and (**D**) CSS.

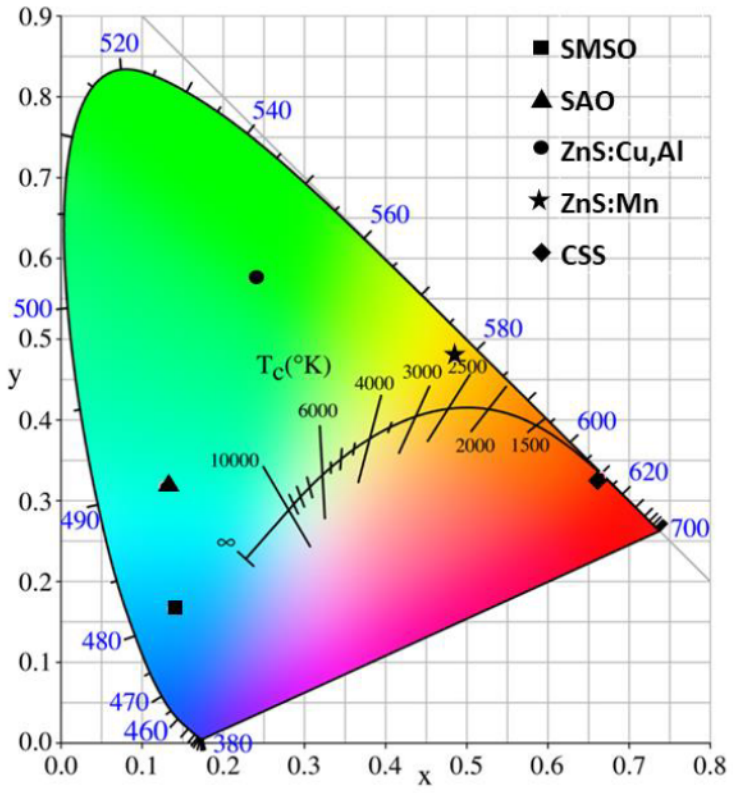


**Fig. S13. CIE chromaticity diagram of five BID-produced nanophosphor colloids.**

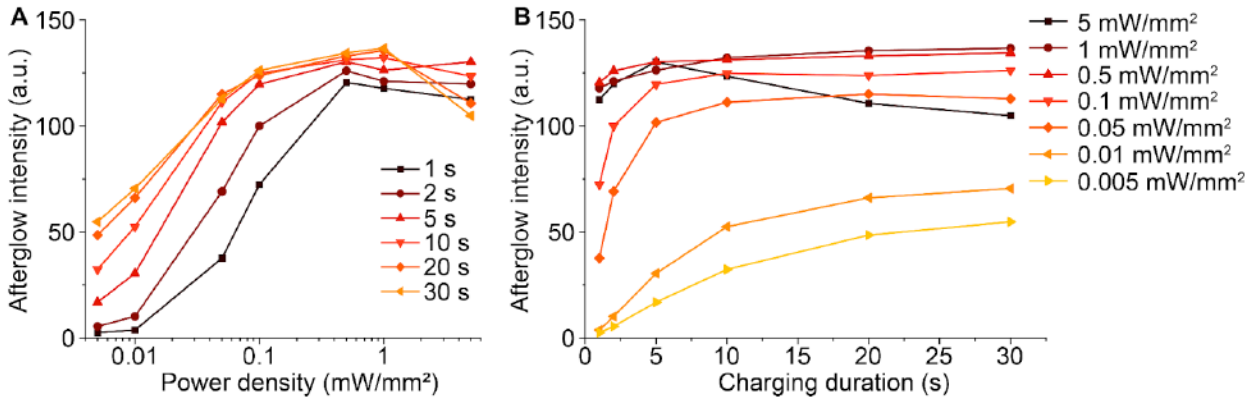


**Fig. S14. Optimization of the afterglow intensity of the SMSO colloid by varying the power density and duration of recharging.** The afterglow intensity is plotted against the recharging power density and duration in (**A**) and (**B**), respectively.

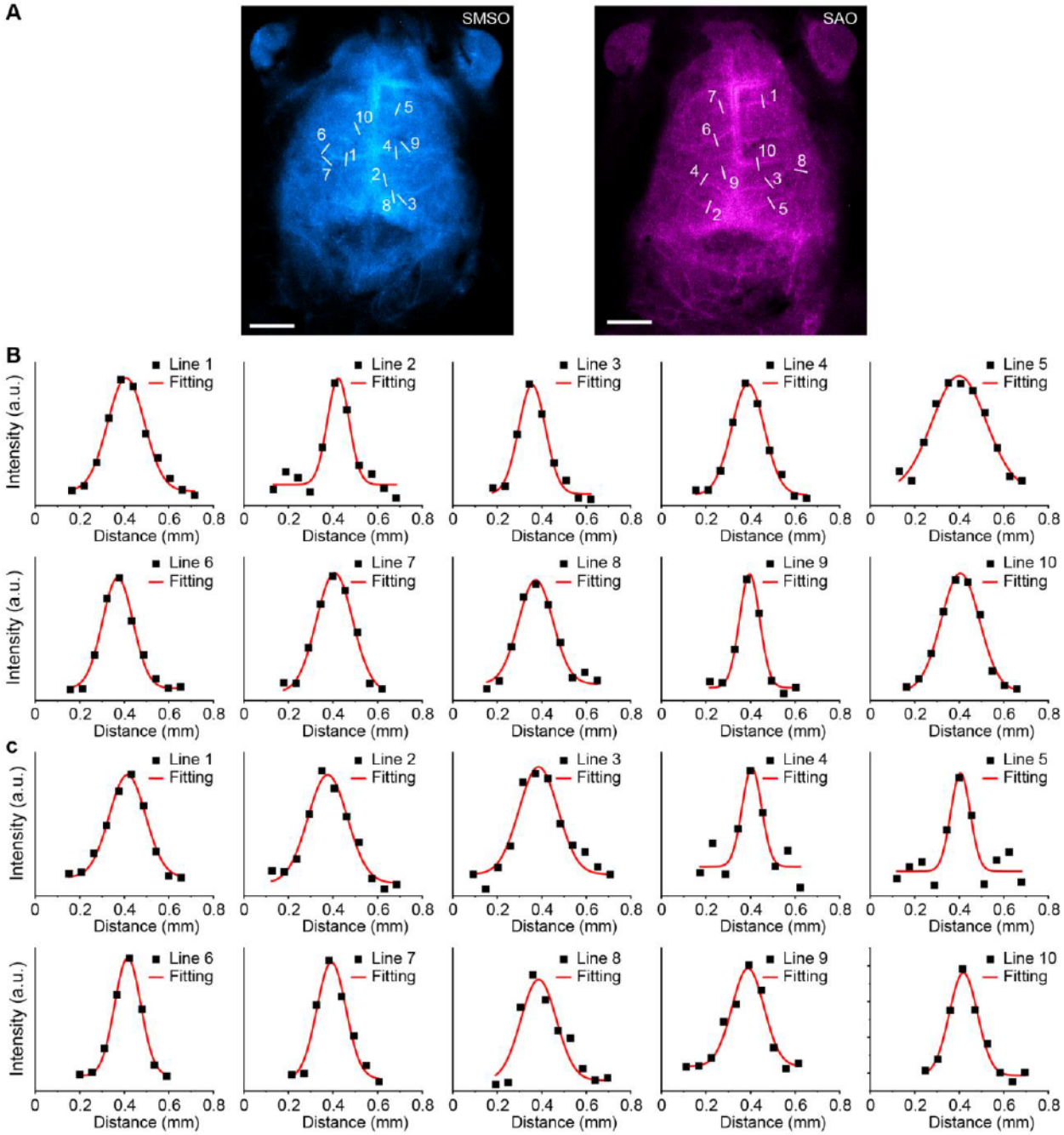


**Fig. S15. Vessel width analysis of transcranial afterglow brain imaging.** (**A**) Transcranial afterglow images of brain vessels after intravenous injection of SMSO (left) and SAO (right) colloidal solutions. Vessels used for width analysis are highlighted with short white lines. Scale bars represent 2.5 mm. (**B,C**) Raw and fitted line profiles for the SMSO (**B**) and SAO (**C**) afterglow images in (**A**).

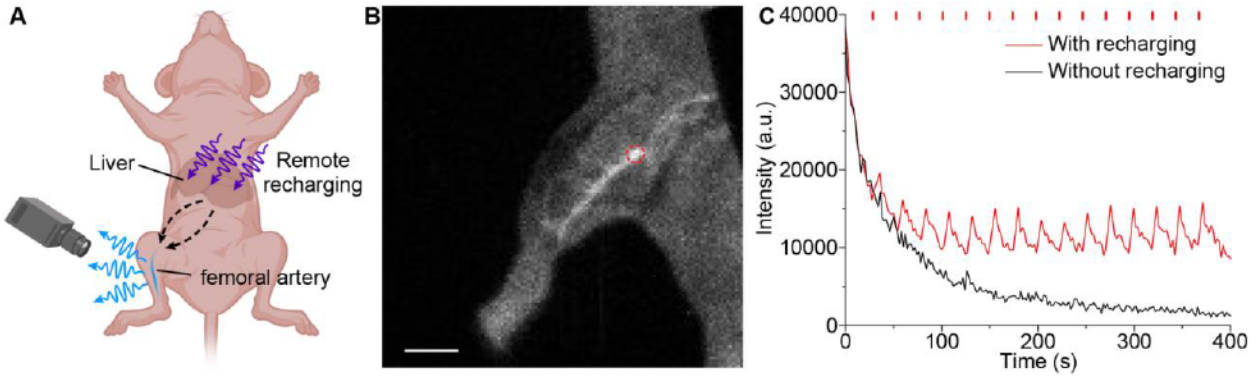


**Fig. S16. Remote recharging of circulating nanophosphor colloids *in vivo*.** (**A**) Schematic showing remote recharging of circulating nanophosphor colloids in hepatic vessels and afterglow imaging of the femoral artery in the mouse hindlimb. The intrinsic circulatory system of the mouse brings the charged nanophosphors in the hepatic vessels to the femoral artery. (**B**) An afterglow image of the femoral artery. The dashed red circle highlights the region for analyzing the afterglow intensity dynamics. The scale bar represents 5 mm. (**C**) Afterglow intensity dynamics of the femoral artery with (red) or without (black) remote recharging in hepatic vessels. The red ticks above the plot represent periodic remote recharging events.

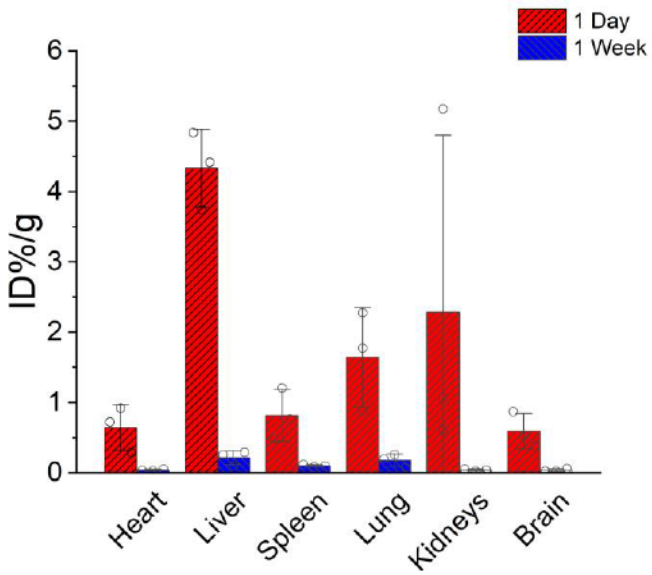


**Fig. S17. Biodistribution of systemically delivered SMSO colloids (493 nmol/L) in major organs on one day (red bars) and one week (blue bars) post-injection.** All data are presented as mean values +/- SD, with individual data shown in open circles. $n = 3$ mice for both time points.

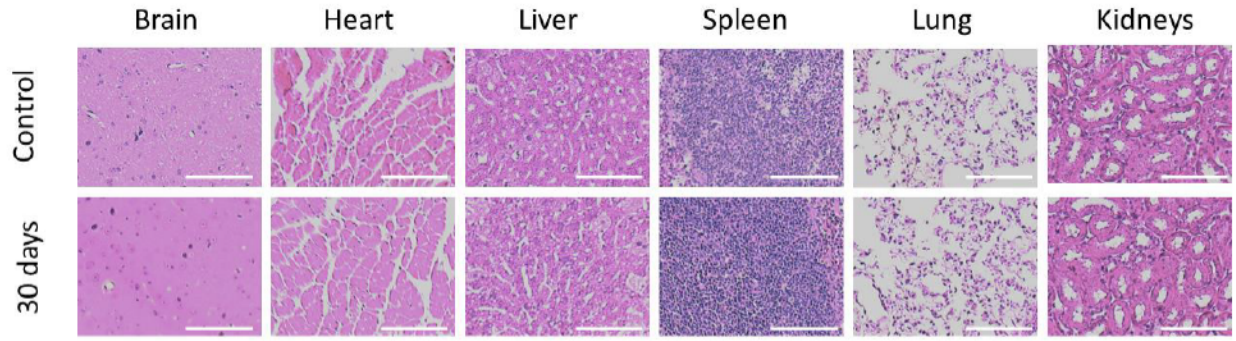


**Fig. S18. Histological analysis of mouse organs.** H&E stained images of major mouse organs 30 days after intravenous injection of an SMSO colloidal solution (493 nmol/L, bottom row), in comparison with those from the control group (top row). No noticeable tissue damage or pathological lesion was found in organs of colloid-injected mice. Scale bars represent 100 μm.

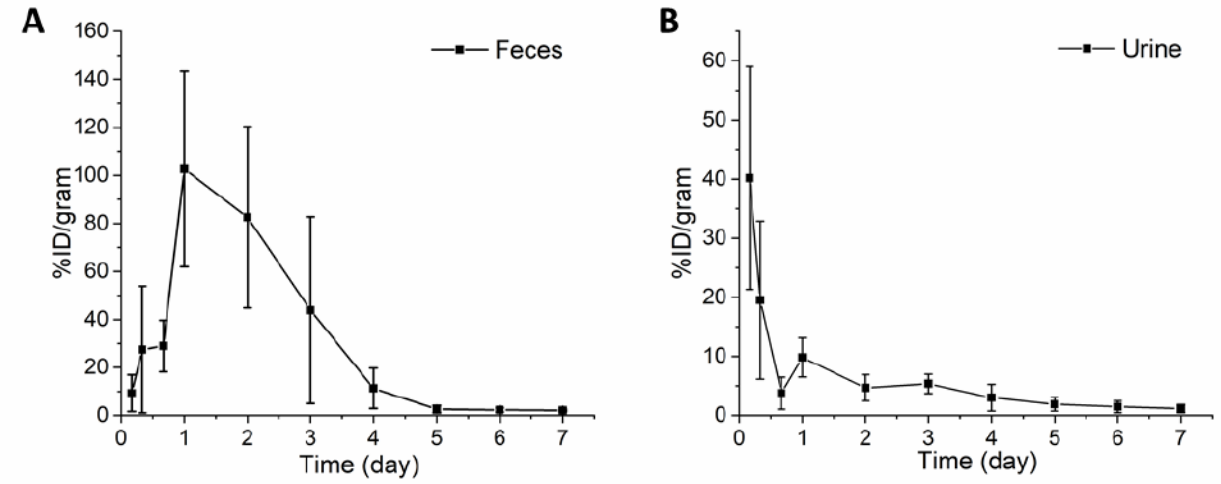


**Fig. S19. Clearance study of SMSO nanophosphor colloids *in vivo*.** The excretion profile of intravenously injected SMSO colloids in the feces (**A**) and urine (**B**) All data are presented as mean values +/- SD. ($n$ = 3 mice).

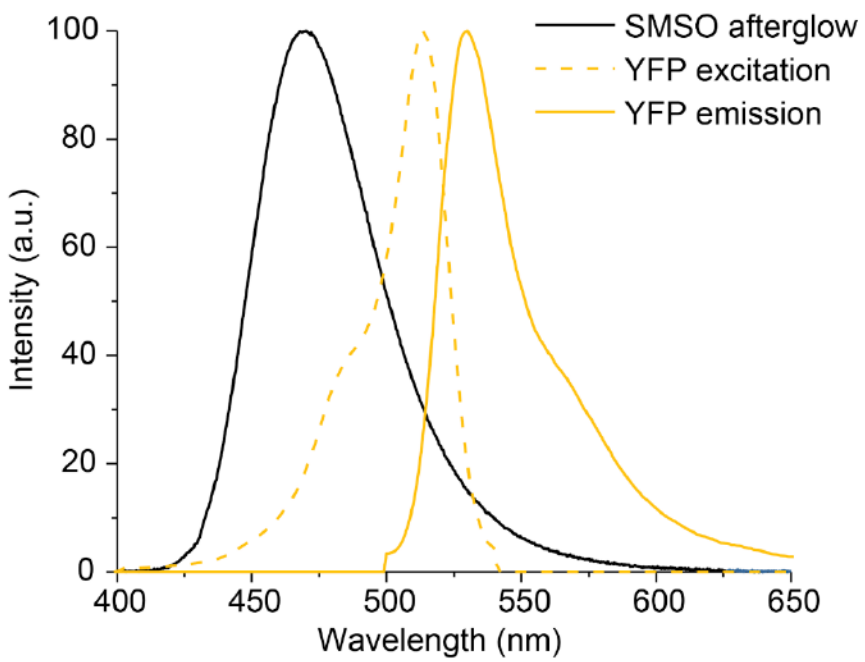


**Fig. S20. The afterglow spectrum of SMSO colloid overlaid with the excitation and emission spectra of the YFP.**

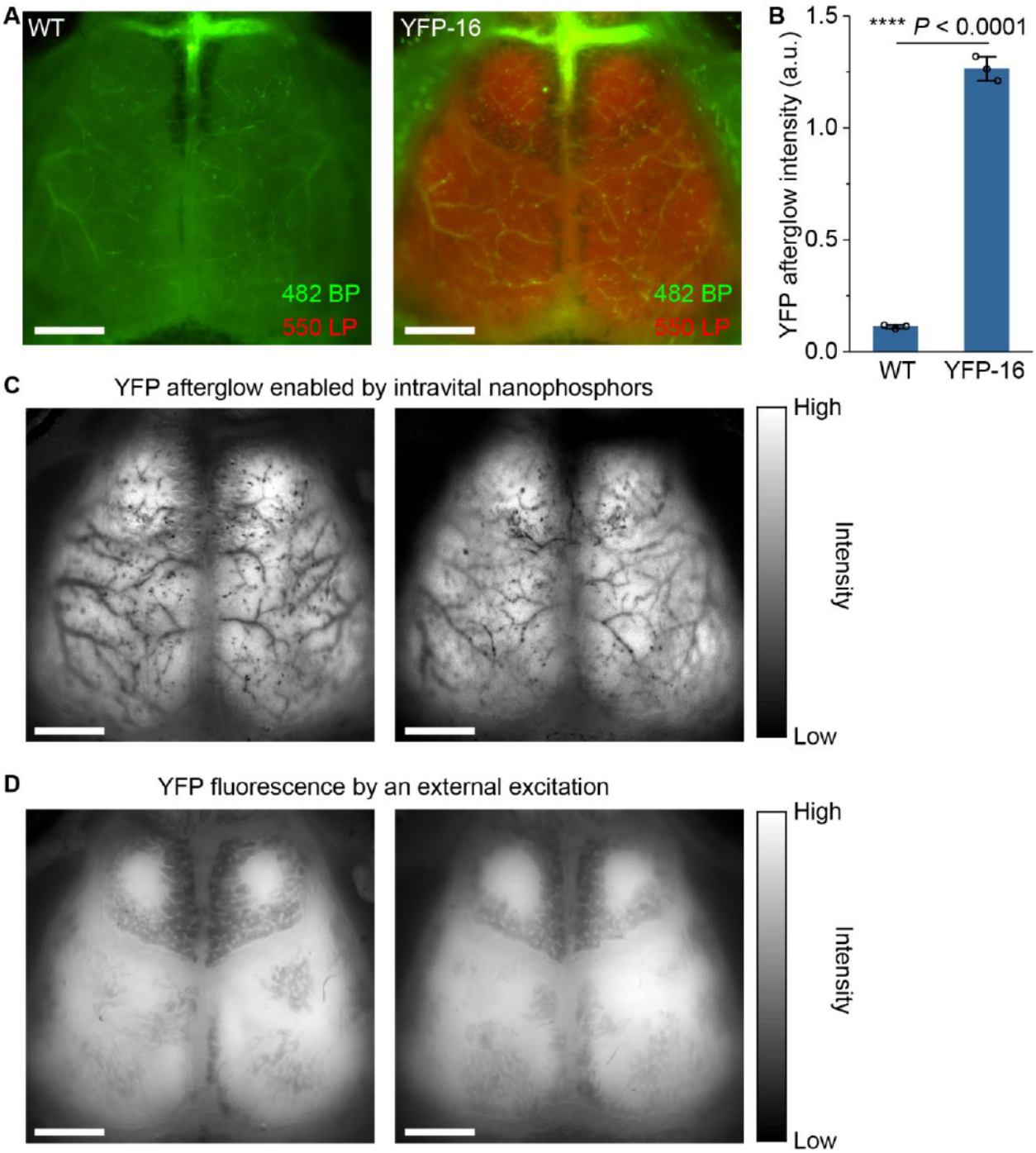


**Fig. S21. YFP imaging with intravital and external excitation sources.** (**A**) Overlay of raw afterglow images collected with 482BP (green, collecting SMSO afterglow only) or 550LP (red, collecting YFP afterglow only) filters in the brains of WT (left) and YFP-16 (right) mice in Fig. 5D. (**B**) Statistical analysis of YFP afterglow intensity of WT and YFP-16 mice in Fig. 5D. All data are presented as mean values +/- SD. $n = 3$ for all groups. (One-way ANOVA, $F(1,4) = 1344.12$, $P < 0.0001$). (**** $P < 0.0001$) (**C,D**) Additional YFP afterglow images via an intravital light source (**C**) and YFP fluorescence images via an external excitation (**D**) in the brains of two additional YFP-16 mice. All scale bars represent 2 mm.

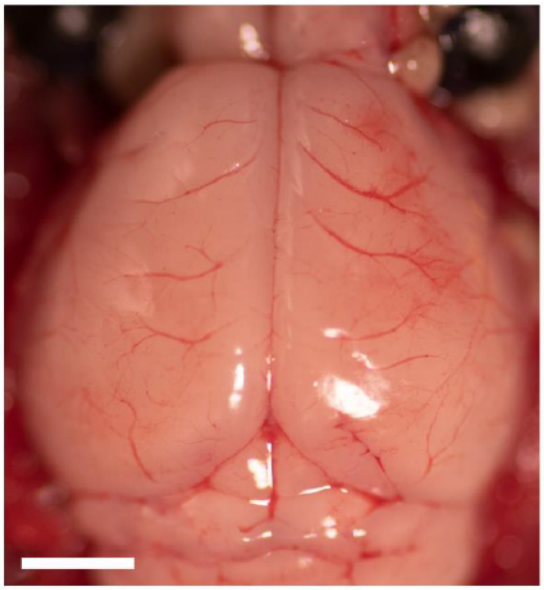

**Fig. S22. Photo of the mouse brain shown in Fig. 5B after removing the skull.** The scale bar represents 2 mm.

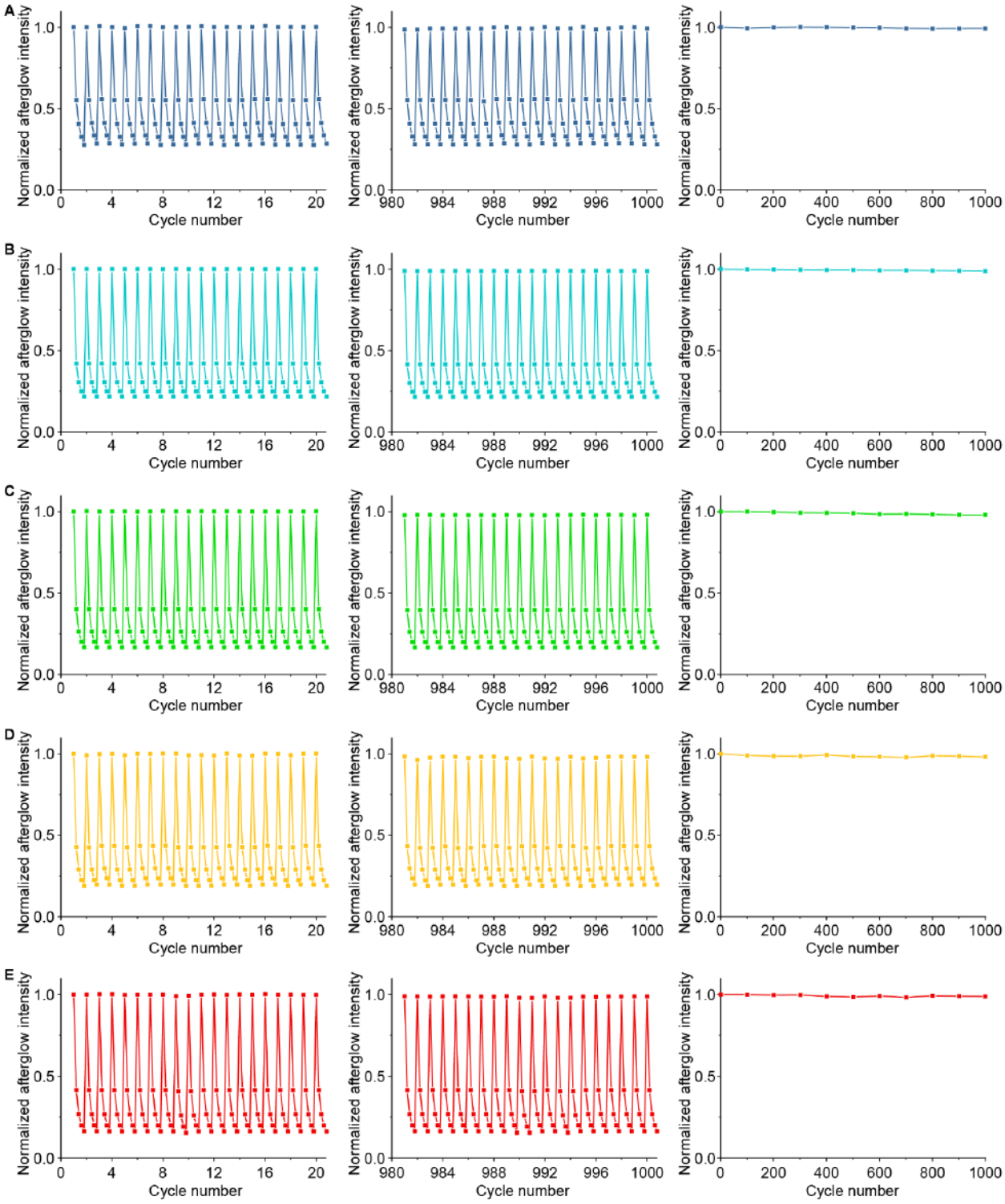


**Fig. S23. Photostability of nanophosphor colloids.** The afterglow intensity of SMSO (**A**), SAO (**B**), ZnS:Cu,Al (**C**), ZnS:Mn (**D**), and CSS (**E**) in the first 20 (left), last 20 (middle), and every 100 (right) recharging cycles.

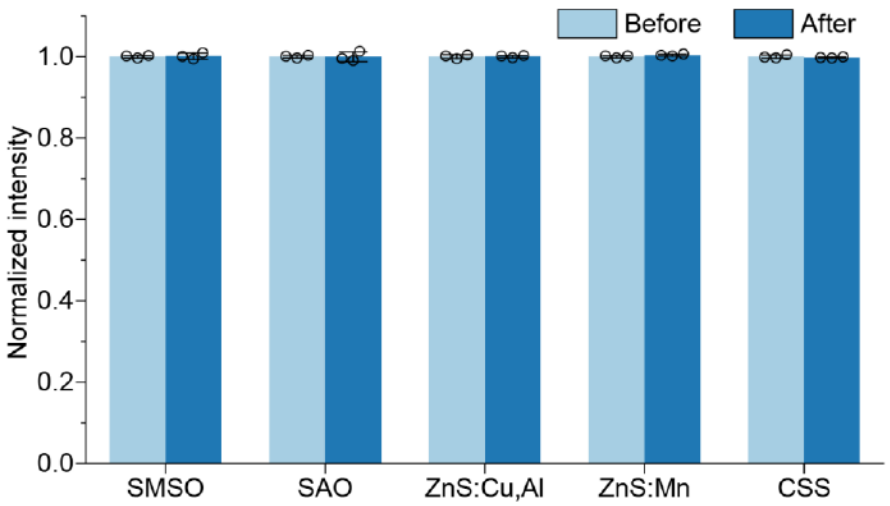


**Fig. S24. Normalized intensity of SMSO, SAO, ZnS:Cu,Al, ZnS:Mn, and CSS before and after 24-hr continuous bleaching by 1 mW/mm$^2$ 365-nm light.** The data are represented as mean ± SD. $n$ = 3 for all groups.

**Table S2. Comparison of BID-produced nanophosphors with previous reports.**

| | Materials | Emission Wavelength | Half-life Time | *In vivo* afterglow intensity of subcutaneous injection | *Ex vivo* afterglow intensity | Sizes | References |
|---|---|---|---|---|---|---|---|
| **Inorganic Persistent Phosphors** | | | | | | | |
| 1 | $Sr_2MgSi_2O_7$:Eu,Dy | 470 nm | 60 s | $1.9 \times 10^9$ p/s/cm$^2$/sr/(mg/mL) | $2.0 \times 10^{10}$ p/s/cm$^2$/sr/(mg/mL) | 43±12nm | This study |
| | $Sr_4Al_{14}O_{25}$:Eu,Dy | 490 nm | 77 s | $3.8 \times 10^{10}$ p/s/cm$^2$/sr/(mg/mL) | $6.2 \times 10^{11}$ p/s/cm$^2$/sr/(mg/mL) | 69±19 nm | |
| | ZnS:Cu,Al | 534 nm | 52 s | $7.5 \times 10^8$ p/s/cm$^2$/sr/(mg/mL) | $3.6 \times 10^9$ p/s/cm$^2$/sr/(mg/mL) | 56±9 nm | |
| | ZnS:Mn | 578 nm | 56 s | $6.8 \times 10^8$ p/s/cm$^2$/sr/(mg/mL) | $3.2 \times 10^9$ p/s/cm$^2$/sr/(mg/mL) | 88±22 nm | |
| | $Ca_{0.85}Sr_{0.15}S$:Eu,Tm | 650 nm | 52 s | $3.0 \times 10^8$ p/s/cm$^2$/sr/(mg/mL) | $1.4 \times 10^9$ p/s/cm$^2$/sr/(mg/mL) | 86±26 nm | |
| 2 | $SiO_2/CdSiO_3$: $In^{3+}$ | 438 nm | ~25 s | ~1 x $10^7$ (p/s/cm$^2$/sr)/(mg/mL) | Absolute intensity not reported for *ex vivo* imaging | ~70 nm | (70) |
| | $SiO_2/CdSiO_3$: $In^{3+}$,$Mn^{2+}$ | 580 nm | ~35 s | ~5 x $10^7$ (p/s/cm$^2$/sr)/(mg/mL) | | | |
| | $SiO_2/CdSiO_3$: $In^{3+}$,$Tb^{3+}$ | 549 nm | ~35 s | ~4 x $10^7$ (p/s/cm$^2$/sr)/(mg/mL) | | | |

| | | | | | | | |
|---|---|---|---|---|---|---|---|
| | $SiO_2$/$CdSiO_3$: $In^{3+}$,$Dy^{3+}$ | 578 nm | ~45 s | Subcutaneous injection not performed | | | |
| 3 | $ZnGa_2O_4$:$Cr_{0.004}$ | 696 nm | ~60 s | ~5 x $10^6$ (p/s/$cm^2$/sr) /(mg/mL) | ~4 x $10^7$ (p/s/$cm^2$/sr) /(mg/mL) | ~9 nm | (17) |
| 4 | $Ca_{0.2}Zn_{0.9}Mg_{0.9}Si_2O_6$: $Eu^{2+}$, $Dy^{3+}$, $Mn^{2+}$ | 690 nm | ~60 s | ~5 x $10^5$ (p/s/$cm^2$/sr) /(mg/mL) | *Ex vivo* imaging not performed | 50-100 nm | (18) |
| 5 | $ZnGa_2O_4$:$Cr^{3+}$-BSA-TAMRA | 702 nm | ~2 s | ~6 x $10^6$ (p/s/$cm^2$/sr) /(mg/mL) | *Ex vivo* imaging not performed | 59 nm | (10) |
| 6 | $ZnGa_{1.995}Cr_{0.005}O_4$ | 695 nm | ~200 s (excited with 5700 lumen LED array); ~1000 s (exited with 6W UV lamp) | Subcutaneous injection not performed | *Ex vivo* imaging not performed | 80 nm | (8) |
| 7 | Si-Pc functionalized $Zn_{1.25}Ga_{1.5}Ge_{0.25}O_4$:0.5%$Cr^{3+}$,2.5%$Yb^{3+}$, 0.25%$Er^{3+}$ Core@$hSiO_2$@CCM | 695 nm | ~15 s | Subcutaneous injection not performed | Absolute intensity not reported for *ex vivo* imaging | 176 nm | (71) |

| | | | | | | | |
|---|---|---|---|---|---|---|---|
| 8 | $ZnGa_2O_4:Cr^{3+}/Sn^{4+}$@MSNs-PEG | 695 nm | ~15 s | Absolute intensity not reported for subcutaneous afterglow imaging. | Absolute intensity not reported for *ex vivo* imaging. | 103 nm | (72) |
| 9 | HA-$Gd_2O_3$-$ZnGa_2O_4:Cr^{3+}$ | 695 nm | ~10 s | Subcutaneous injection not performed. | Absolute intensity not reported for *ex vivo* imaging. | 142 nm | (73) |
| 10 | c(RGDyK)-PEG-$Zn_{2.94}Ga_{1.96}Ge_2O_{10}:Cr^{3+},Pr^{3+}$ | 700 nm | ~seconds | Absolute intensity not reported for subcutaneous afterglow imaging. | Absolute intensity not reported for *ex vivo* imaging | 132 nm | (74) |
| 11 | Raspberry-like mesoporous $Zn_{1.07}Ga_{2.34}Si_{0.98}O_{6.56}:Cr_{0.01}$ | 698 nm | ~100 s | Subcutaneous injection not performed | Absolute intensity not reported for *ex vivo* imaging | ~110 nm | (75) |

| | | | | | | | |
|---|---|---|---|---|---|---|---|
| 12 | Folate acid-functionalized $Zn_{1.25}Ga_{1.5}Ge_{0.25}O_4$:0.5%$Cr^{3+}$,2.5%$Yb^{3+}$, 0.25%$Er^{3+}$ | 691 nm | ~350 s | Absolute intensity not reported for subcutaneous afterglow imaging | *Ex vivo* imaging not performed | 44 nm | (76) |
| 13 | $mSiO_2$@$Gd_3Ga_5O_{12}$:$Cr^{3+}$, $Nd^{3+}$ | 745 nm | ~30 s | Absolute intensity not reported for subcutaneous afterglow imaging | Absolute intensity not reported for *ex vivo* imaging | 50 nm | (77) |
| 14 | $Zn_{1+x}Ga_{2-2x}Ge_xO_4$:$Cr^{3+}$@zeolitic imidazolate framework-8 | 699 nm | ~40 s | Subcutaneous injection not performed | Absolute intensity not reported for *ex vivo* imaging | 100-200 nm | (78) |
| 15 | $LaAlO_3$:$Cr^{3+}$,$Sm^{3+}$ | 735 nm and 750 nm | ~60 s | Subcutaneous injection not performed | *Ex vivo* intensity measurement not performed on the suspension of nanoparticles | <100 nm | (79) |
| 16 | $ZnGa_2O_4Cr_{0.004}$ | 696 nm | ~90 s | Subcutaneous injection not performed | Absolute intensity not reported for *ex vivo* | 10 nm | (80) |

| | | | | | | | |
|---|---|---|---|---|---|---|---|
| | | | | | imaging | | |
| 17 | $CaMgSi_2O_6$ :$Eu^{2+}$,$Mn^{2+}$, $Pr^{3+}$ | 685 nm | ~270 s | Subcutaneous injection not performed | *Ex vivo* imaging not performed | | (81) |
| 18 | Core–shell-structured Ln-doped $NaY(Gd)F_4$ (Ln = $Nd^{3+}$, $Ho^{3+}$, $Tm^{3+}$, $Er^{3+}$) | 1064 nm ($Nd^{3+}$) | ~250 s | Subcutaneous injection not performed | Absolute intensity not reported for *ex vivo* imaging | 42 nm | (16) |
| | | 1180 nm ($Ho^{3+}$) | ~200 s | | | | |
| | | 1475 nm ($Tm^{3+}$) | ~100 s | | | | |
| | | 1525 nm ($Er^{3+}$) | ~100 s | | | | |
| 19 | $ZnGa_2O_4$:Cr | 700 nm | ~180 s | Absolute intensity not reported for subcutaneous afterglow imaging | Absolute intensity not reported for *ex vivo* imaging | 141 nm | (82) |
| 20 | ($Zn_2SiO_4$:Mn):$Y^{3+}$, $Yb^{3+}$, $Tm^{3+}$ | 525 nm | ~420 s | Subcutaneous injection not performed | Concentration of nanoparticles not reported for *ex vivo* imaging | 120-160 nm | (83) |

| | | | | | | | |
|---|---|---|---|---|---|---|---|
| 21 | $CaSnO_3:Bi^{2+}$ | 810 nm | ~970 s | Subcutaneous injection not performed | Absolute intensity not reported for *ex vivo* imaging | 50-100 nm | (84) |
| 22 | $LiGa_5O_8:Cr^{3+}$ | 716 nm | ~2900 s | ~2 x $10^6$ (p/s/$cm^2$/sr) /(mg/mL) | ~2 x $10^6$ (p/s/$cm^2$/sr) /(mg/mL) | 50-150 nm | (19) |
| 23 | $Zn_{1.1}Ga_{1.8}Ge_{0.1}O_4$:0.5% Cr core and β-$NaYbF_4$:Tm@$NaYF_4$ shell nanocluster | 700 nm | ~5 s | Subcutaneous injection not performed | Absolute intensity not reported for *ex vivo* imaging | ~100 nm | (39) |
| **Organic Persistent Phosphors** | | | | | | | |
| 24 | SPPVN | 780 nm | 288 s | ~1.0 x $10^7$ (p/s/$cm^2$/sr) /(mg/mL) | ~1.2 x $10^8$ (p/s/$cm^2$/sr) /(mg/mL) | 24 nm | (85) |
| 25 | MEHPPV-based SPN-NCBS | 780 nm | 396 s | ~5.7 x $10^8$ (p/s/$cm^2$/sr) /(mg/mL) | ~1.8 x $10^9$ (p/s/$cm^2$/sr) /(mg/mL) | 40 nm | (9) |
| 26 | DPhCzT-based OSN-T / OSN-B | 530 nm | <1 s | ~1.3 x $10^7$ (p/s/$cm^2$/sr) /mM | ~1.3 x $10^7$ (p/s/$cm^2$/sr) /mM | 20-60 nm | (86) |
| 27 | PFVA-NCBS-DO | 780 nm | ~180 s | ~1.8 x $10^8$ (p/s/$cm^2$/sr) /(mg/mL) | ~1.1 x $10^{10}$ (p/s/$cm^2$/sr) /(mg/mL) | ~125 nm | (11) |
| 28 | Sodium alginate gel loaded with PdPc(OBu) | 613 nm | ~1 s | ~2.2 x $10^2$ (p/s/$cm^2$/sr) /(mg/mL) | ~2.2 x $10^2$ (p/s/$cm^2$/sr) /(mg/mL) | ~100 nm | (87) |

| | | | | | | | |
|---|---|---|---|---|---|---|---|
| | 8-4-(5,6-dihydro-2-phenyl-1,4-oxathiin-3-yl)-N,N-dimethylbenzenamine-Eu(TPPO)$_2$(β-NTA)-based nanoparticles | | | | | | |
| 29 | Si-Pc-CUEM afterglow nanoparticles | 613 nm | ~1.5 s | Absolute intensity not reported for subcutaneous afterglow imaging | Absolute intensity not reported for *ex vivo* imaging | ~225 nm | (14) |
| 30 | UCANPs@RAW | 615 nm | ~17 s | Absolute intensity not reported for subcutaneous afterglow imaging | Absolute intensity not reported for *ex vivo* imaging | ~320 nm | (88) |
| 31 | AGL AIE dots | 650 nm | ~2880 s | Subcutaneous injection not performed | ~1.5 x $10^8$ (p/s/cm$^2$/sr) /(mg/mL) | ~95 nm | (89) |

Abbreviations: PEG: polyethylene glycol; BSA: bovine serum albumin; TAMRA: 5-carboxy-tetramethylrhodamine; Si-Pc: silicon phthalocyanine; hSiO$_2$: hollow silica; CCM: cancer cell membrane; MSNs: mesoporous silica nanoparticles; HA: hyaluronic acid; c(RGDyK): cyclic arginine-glycine-aspartic acid-tyrosine-lysine pentapeptide; mSiO$_2$: mesoporous silica; PPV: amphiphilic poly(*p*-phenylenevinylene); SPPVN: self-assembled amphiphilic poly(*p*-phenylenevinylene) nanoagents; MEHPPV: poly[2-methoxy-5-(2-ethylhexyloxy)-1,4-phenylene] end-capped with dimethylphenyl ; SPN:semiconducting polymer nanoparticles; NCBS: silicon 2,3-naphthalocyanine bis(trihexylsilyloxide); DPhCzT: 4,6-Diphenyl-2-carbazolyl-1,3,5-triazine; OSN-T/B: organic semiconducting nanoparticles synthesized via Top-down/Bottom-up approach;

PFVA: poly[(9,9′-dioctyl-2,7-divinylenefluorenylene)-alt-(9,10-anthracene)]; DO: (N,N-dimethyl-4-(3-phenyl-5,6-dihydro-1,4-dioxin-2-yl)aniline); $PdPc(OBu)_8$: 1,4,8,11,15,18,22,25-octabutoxyphthalocyaninato-palladium(II); TPPO: Triphenylphosphine oxide: NTA: nitrilotriacetic acid; UCANPs@RAW: $PdPc(OBu)_8$, 4-(5,6-dihydro-2-phenyl-1,4-oxathiin-3-yl)-N,N-dimethylbenzenamine, and $Eu(TTA)_3Phen$-based macrophage-camouflaged afterglow nanocomplex; AGL: afterglow luminescent; AIE: aggregation-induced emission.